Angewandte International Edition Chemie
www.angewandte.org

How to cite: *Angew. Chem. Int. Ed.* **2022,** *61,* e202200947
International Edition: doi.org/10.1002/anie.202200947
German Edition: doi.org/10.1002/ange.202200947

Gas Separation **Hot Paper**

Comprehensive Pore Tuning in an Ultrastable Fluorinated Anion Cross-Linked Cage-Like MOF for Simultaneous Benchmark Propyne Recovery and Propylene Purification

Yunjia Jiang[+]*, Jianbo Hu*[+]*, Lingyao Wang*[+]*, Wanqi Sun, Nuo Xu, Rajamani Krishna, Simon Duttwyler, Xili Cui, Huabin Xing, and Yuanbin Zhang**

Abstract: Propyne/propylene (C_3H_4/C_3H_6) separation is an important but challenging industrial process to produce polymer-grade C_3H_6 and recover high-purity C_3H_4. Herein, we report an ultrastable TiF_6^{2-} anion cross-linked metal–organic framework (ZNU-2) with precisely controlled pore size, shape and functionality for benchmark C_3H_4 storage (3.9/7.7 mmol g^{-1} at 0.01/1.0 bar and 298 K) and record high C_3H_4/C_3H_6 (10/90) separation potential (31.0 mol kg^{-1}). The remarkable C_3H_4/C_3H_6 (1/99, 10/90, 50/50) separation performance was fully demonstrated by simulated and experimental breakthroughs under various conditions with excellent recyclability and high productivity (42 mol kg^{-1}) of polymer-grade C_3H_6 from a 1/99 C_3H_4/C_3H_6 mixture. A modelling study revealed that the symmetrical spatial distribution of six TiF_6^{2-} on the icosahedral cage surface provides two distinct binding sites for C_3H_4 adsorption: one serves as a tailored single C_3H_4 molecule trap and the other boosts C_3H_4 accommodation by cooperative host–guest and guest–guest interactions.

Introduction

Propylene (C_3H_6) is a fundamental olefin for the production of various chemicals and polymers such as polypropylene, acrylonitrile and propylene oxide.[1] Its global production capacity had reached 140 million tons in 2020, second only to ethylene (C_2H_4). It is mainly produced from the cracking of naphtha or the fractional distillation of hydrocarbons and is inevitably mixed with a small amount ($\leq 10\,\%$) of propyne (C_3H_4), which severely poisons the catalysts used in propylene polymerization.[2] To meet the demand of propylene polymerization, the C_3H_4 content must be reduced to ≤ 40 ppm. Currently, the dominant technique used to remove C_3H_4 is selective hydrogenation with noble-metal catalysts, which usually suffers from several disadvantages, including the high cost and short lifetime of the catalysts, low efficiency, and potential secondary pollution caused by over-hydrogenation. On the other hand, C_3H_4 that can be produced by thermal or catalytic pyrolysis of C_3H_6 is also an important feedstock used as speciality fuel and chemical intermediate.[3] To recover C_3H_4, solvent extraction is the current state-of-the-art technology, which is associated with pollution. Therefore, it is significant and imperative to develop new approaches to efficiently separate C_3H_4/C_3H_6.

Adsorption-based separation technologies are attracting widespread attention owing to the eco-friendly nature and energy efficiency.[4] Recently, metal–organic frameworks (MOFs) with designable pore size and chemistry have emerged as a new class of porous materials for efficient gas separation.[5] Many MOFs with excellent separation performance for CO_2/N_2,[6] CO_2/CH_4,[7] C_2H_2/CO_2,[8] C_2H_2/C_2H_4[9] or C_2H_4/C_2H_6[10] have been developed. When compared, the C_3H_4/C_3H_6 separation is more challenging and less developed due to the higher similarity in polarity and molecular size (C_3H_4: 4.16×4.01×6.51 Å^3, C_3H_6: 4.65×4.16×6.44 Å^3, Table S2).[11]

In many fields, hexagonal radar charts are used to display the strengths and weaknesses quantitatively (Figure S52), which can be referenced to evaluate the potential of porous materials for C_3H_4 recovery and C_3H_6 purification in C_3H_4/C_3H_6 separation based on the physical properties of adsorbents prior to the practical utilization. In this context, the following six metrics should be considered: normal pressure C_3H_4 capacity ($q_{100\,\mathrm{kPa}}$), low pressure C_3H_4 capacity ($q_{1\mathrm{kPa}}$), IAST selectivity (S), adsorption heat (Q_{st}), thermal stability, and stability towards water and humid air (Sche-

---

[*] Y. Jiang,[+] Dr. L. Wang,[+] W. Sun, N. Xu, Prof. Y. Zhang
Key Laboratory of the Ministry of Education for Advanced Catalysis Materials, College of Chemistry and Life Sciences
Zhejiang Normal University
Jinhua 321004 (P.R. China)
E-mail: ybzhang@zjnu.edu.cn

Dr. J. Hu,[+] Prof. X. Cui, Prof. H. Xing
Key laboratory of Biomass Chemical Engineering of Ministry of Education, College of Chemical and Biological Engineering, Zhejiang University
Hangzhou 310027 (P.R. China)

Prof. R. Krishna
Van't Hoff Institute for Molecular Sciences
University of Amsterdam
Science Park 904, 1098 Amsterdam (The Netherlands)

Prof. S. Duttwyler
Department of Chemistry, Zhejiang University
Hangzhou 310027 (P.R. China)

[+] These authors contributed equally to this work.

me 1A). The higher $q_{100\,\text{kPa}}$ and $q_{1\text{kPa}}$ usually provide enhanced C_3H_4 storage ability, but may also lead to high C_3H_6 uptake and finally result in lower C_3H_4/C_3H_6 selectivity. Low Q_{st} is preferred for the regeneration of the adsorbent, but is usually associated with weak affinity towards C_3H_4 and unsatisfactory selectivity. Excellent thermal and chemical stability of the adsorbents is definitely required to handle the complicated practical conditions but still difficult to achieve in most MOFs. To the best of our knowledge, none have discovered a porous material with high C_3H_4 capacity ($q_{100\,\text{kPa}} > 7\ \text{mmol}\,\text{g}^{-1}$; $q_{1\text{kPa}} > 3\ \text{mmol}\,\text{g}^{-1}$), high selectivity ($S > 10$), low adsorption heat ($Q_{\text{st}} < 45\ \text{kJ}\,\text{mol}^{-1}$) as well as excellent thermal and chemical stability.

MOFs with abundant open metal sites (OMS) and cage nanopores (7–15 Å) such as Cu-BTC provide large C_3H_4 capacity under normal pressure due to the large pore volume and high binding affinity towards C_3H_4 but fail to effectively separate C_3H_4/C_3H_6 because of the low selectivity (Scheme 1B).[12] Anion hybrid ultramicroporous materials with contracted 1D channel (<7 Å) give extremely high C_3H_4/C_3H_6 separation selectivity but low storage capacity, such as SIFSIX-3-Ni and SIFSIX-2-Cu-i (Scheme 1C).[13] Besides, many MOFs with OMS or SiF_6^{2-} functionality are not resistant to humid air, not to mention the direct contact with water or acidic gas vapor.[14] Therefore, it is urgently needed but still highly difficult to develop MOFs with desired metrics to tackle the dilemma.

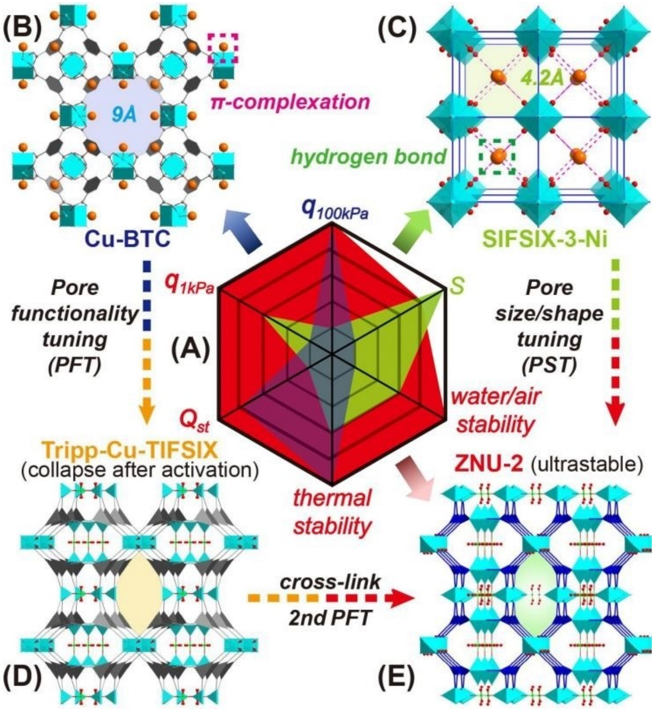

Scheme 1. Illustration of tuning pore size/shape/functionality to achieve high C_3H_4 storage capacity ($q_{100\text{kpa}}$, $q_{1\text{kpa}}$), good C_3H_4/C_3H_6 selectivity (S), excellent stability and modest adsorption heat (Q_{st}) in ZNU-2. A) A radar chart for comprehensive comparison of the C_3H_4 storage and C_3H_4/C_3H_6 separation performance. B–E) Structures and characteristics of Cu-BTC, SIFSIX-3-Ni, Tripp-Cu-TIFSIX and ZNU-2. Orange balls represent potential C_3H_4 adsorption sites in B and C.

In 2016, Zaworotko reported the first example of TiF_6^{2-} hybrid cage-like MOF Tripp-Cu-TIFSIX that combines a large theoretical pore volume and fluorinated anion functionality (Scheme 1D), which seemed to be promising to balance the C_3H_4 capacity and C_3H_4/C_3H_6 selectivity.[15] However, Tripp-Cu-TIFSIX is very unstable and collapses after activation probably because only half of the square Cu-pyridyl coordination building blocks are cross-linked by TiF_6^{2-}, leading to an unsaturated penta-coordinating Cu^{II} network. This half cross-linked topology is considered to be resulted from the length mismatch between long tripp (2,4,6-tris(4-pyridyl)pyridine) linker and short TiF_6^{2-} anion pillar. Therefore, we hypothesized that cage-like MOFs with completely TiF_6^{2-} cross-linked topology should be accessible through shortening the length of the tritopic linker and the obtained OMS-free network is potential to be a promising material for C_3H_4 storage and C_3H_4/C_3H_6 separation by combining a large cage pore volume and abundant TiF_6^{2-} anion functional sites. With this in mind, we reported herein a novel TiF_6^{2-} anion cross-linked MOF (ZNU-2) constructed by $CuTiF_6$ and tri(pyridin-4yl)amine (Tripa) for simultaneous benchmark propyne storage and propyne/propylene separation (Scheme 1E). Due to the complete cross-link, ZNU-2 features excellent stability. Static gas adsorption isotherms showed that ZNU-2 takes up 3.9 and 7.7 $\text{mmol}\,\text{g}^{-1}$ of C_3H_4 at 0.01 and 1.0 bar (298 K), respectively. The low pressure (0.01 bar) capacity of C_3H_4 is the highest among all the anion pillared MOFs. The calculated IAST selectivity for C_3H_4/C_3H_6 is 12.5–16.2 (v/v = 1/99–50/50) and the calculated C_3H_4/C_3H_6 (10/90) separation potential (Δq) of 31.0 $\text{mmol}\,\text{g}^{-1}$ is the highest among all the materials in the context of C_3H_4/C_3H_6 separation. Simulated breakthroughs also indicated ZNU-2 exhibits the record high C_3H_6 productivity from the 10/90 C_3H_4/C_3H_6 mixture. Experimental breakthroughs with different C_3H_4/C_3H_6 (1/99,10/90, 50/50) ratios or different flow rates as well as under different temperatures all showed the excellent practical C_3H_4/C_3H_6 separation performance without capacity loss after 10 cycles. Additionally, the breakthrough curves measured under 65 % humidity were entirely consistent with those under dry condition. The calculated Q_{st} is as low as 43.0 $\text{kJ}\,\text{mol}^{-1}$, indicative of its facility for C_3H_4 recovery and regeneration of ZNU-2. Modelling simulation revealed that the symmetrical spatial distribution of six TiF_6^{2-} pillars on the icosahedral pore surface provides two distinct binding sites for C_3H_4 adsorption: one serves as a tight single C_3H_4 molecule trap in the channels connecting two cages and the other boosts C_3H_4 accommodation in the cages by cooperative host–guest and guest–guest interactions. The combination of such multiple functionalities in a single MOF has never been reported previously in porous materials for C_3H_4/C_3H_6 separation.

Results and Discussion

Single crystals of ZNU-2 were cultivated by layering a MeOH solution of Tripa onto an aqueous solution of $CuTiF_6$ (Figure 1A, B). X-ray structural analysis of ZNU-2 revealed that it crystallizes in a three-dimensional (3D) framework in the cubic $Pm\bar{3}n$ space group, similar to Tripp-Cu-TIFSIX with cubic $Pm\bar{3}$ space group.[15] Due to the reduction of the organic linker length from Tripp (triangle side N⋯N length = 9.7 Å) to Tripa (triangle side N⋯N length = 7.3 Å, Figure S6), the length of the unit cell edge decreased from 21.2 Å to 17.6 Å, which is exactly twice of the TiF_6^{2-} cross-linked Cu⋯Cu distance. The Tripa connected Cu⋯Cu distance is 10.8 Å. Such distances are very suitable to form isosceles triangle using Cu as the vertex, which extends to generate an icosahedral Cu cage with a pore aperture of ca. 8.5 Å (Figure 1C, E). This pore aperture is similar to that of SIFSIX-1-Cu (8 Å), which exhibits the highest C_3H_4 uptake among all the anion hybrid porous materials but is not stable in humid air.[13] The cage-like pores are interconnected with each other by contracted necks (≈4 Å, Figure 1D), different from the separated 1D channels in traditional anion pillared MOFs. Such periodically expanded and contracted cage-neck structure may provide different diffusion kinetic for molecules with different shapes and diameters.[10a,12b] Thus, combining abundant fluorinated binding sites for the recognition of C_3H_4/C_3H_6, a large cage pore volume for C_3H_4 accommodation, a completely TiF_6^{2-} cross-linked OMS-free network to enhance the stability as well as small window aperture to enhance C_3H_4/C_3H_6 diffusion kinetic difference, ZNU-2 features a promising structure to offer benchmark C_3H_4 storage capacity and C_3H_4/C_3H_6 separation performance.

Before gas adsorption experiments, we tested the stability of ZNU-2. As shown in Figure 1F–H, ZNU-2 is extremely chemically and thermally stable. Then, N_2 gas adsorption experiments at 77 K were conducted (Figure 2A), which indicated the microporous character of ZNU-2 with pore size distribution in 7.5–9.4 Å, highly close to the pore aperture of ≈8.5 Å calculated from the single-crystal structure. The BET surface area and pore volume are 1380 $m^2\,g^{-1}$ and 0.575 $cm^3\,g^{-1}$, respectively, which allow to accommodate a large amount of gas molecules. This BET surface area is even larger than that of SIFSIX-1-Cu (1128 $m^2\,g^{-1}$)[13] and ranks the highest among all the anion pillared materials.

Single-component C_3H_4 and C_3H_6 adsorption measurements at 298 K were conducted. At 1.0 bar and 298 K, the C_3H_4 and C_3H_6 uptakes were 7.7 and 5.3 $mmol\,g^{-1}$, corresponding to 4.3 C_3H_4 molecules and 3.0 C_3H_6 molecules adsorbed per TIFSIX anion (Figure 2B, C). Such high C_3H_4/TIFSIX ratio means every free F site can bind 1.07 C_3H_4 atoms, similar to that of SIFSIX-1-Cu. This C_3H_4/TIFSIX ratio is much higher than those of SIFSIX-3-Ni (1.09), SIFSIX-14-Cu-i (2.08), TIFSIX-14-Cu-i (2.31), ZU-62 (2.30), and SIFSIX-2-Cu-i (2.57) (Figure 2C). The adsorption capacity under 1 and 10 kPa were further compared with other MOFs. The C_3H_4 uptake at 1 kPa is as high as 3.9 $mmol\,g^{-1}$ while that of C_3H_6 is only 0.61 $mmol\,g^{-1}$ under the same conditions. Such large capacity difference is very

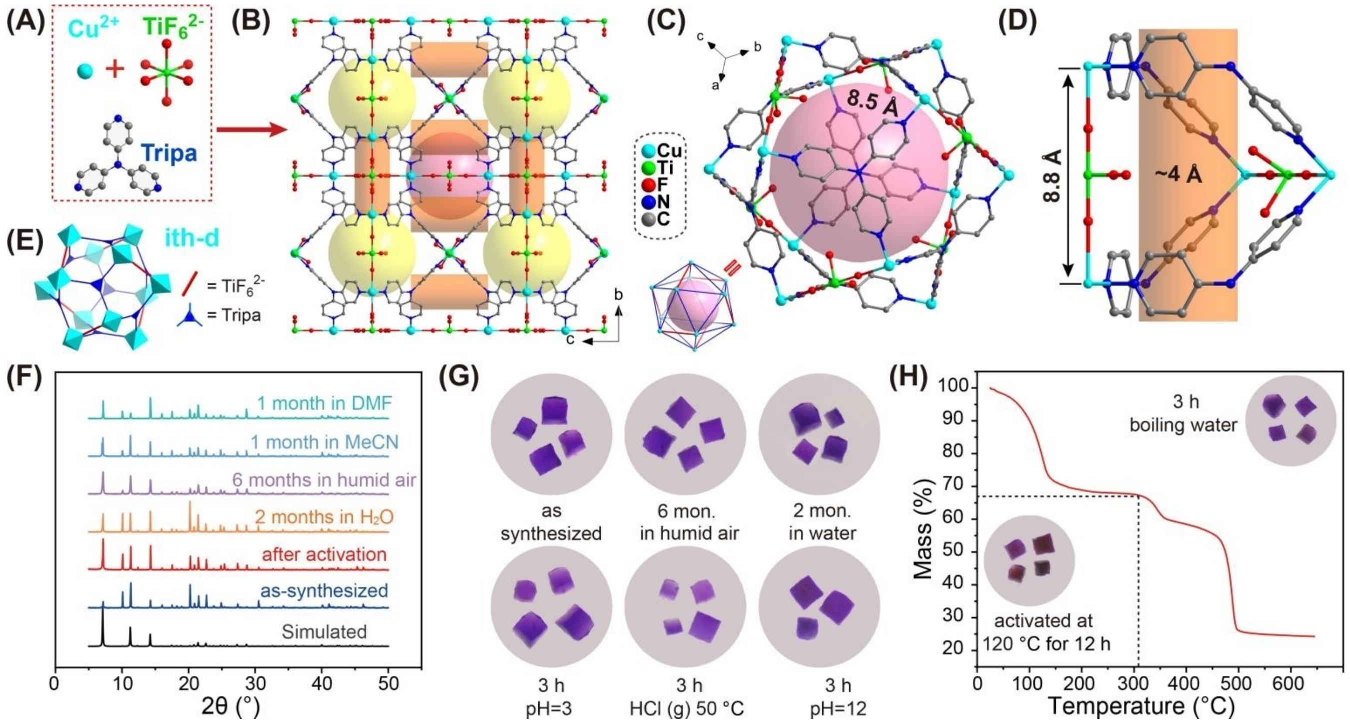

Figure 1. Porous structure and stability test of ZNU-2. A) Basic unit to construct ZNU-2. B) Structure of ZNU-2 with cage-like pores. C) Structure and size of icosahedral Cu^{II} cage. D) structure and aperture of the channel between two cages. E) The ith-d topology of ZNU-2. F) The PXRD patterns under different conditions. G, H) Photographs of single crystals of ZNU-2 after different treatment and the TGA curve.

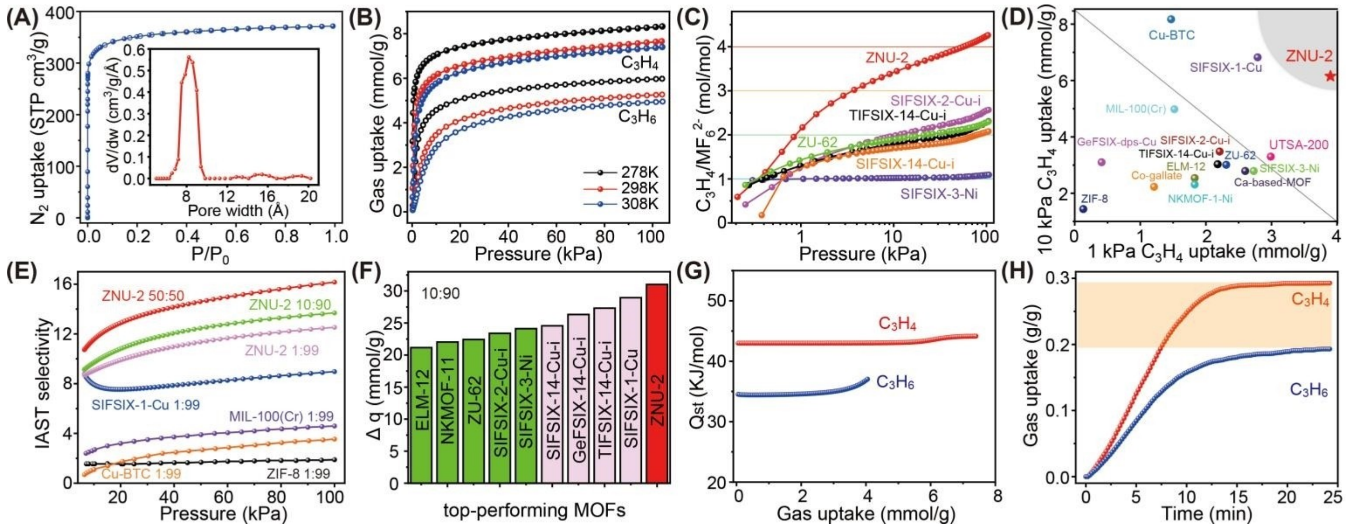

Figure 2. A) N_2 sorption isotherms for ZNU-2 and its calculated pore size distribution. B) C_3H_4 and C_3H_6 adsorption isotherms for ZNU-2. C) Comparison of the C_3H_4 adsorption isotherms of ZNU-2 with fluorinated anion hybrid ultramicroporous materials. D) Comparison of the low-pressure C_3H_4 uptake among top-performing MOFs. E) Comparison of IAST selectivity of ZNU-2 with other MOFs showing high C_3H_4 capacity (>5 mmol g^{-1}). F) Comparison of ZNU-2's IAST-based separation potential ($\Delta q = C_3H_4$ uptake $\times 9 - C_3H_6$ uptake) for C_3H_4/C_3H_6 (10/90) mixtures with reported top performing MOFs. G) The isosteric heat of adsorption, Q_{st}, for C_3H_4 and C_3H_6 in ZNU-2. H) Adsorption kinetic curves of C_3H_4 and C_3H_6 in ZNU-2.

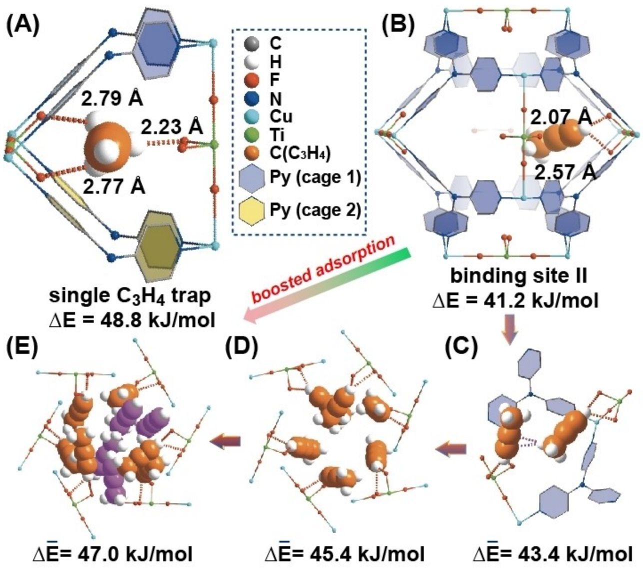

Figure 3. The DFT-D optimized adsorption configuration and bonding energy of C_3H_4 in ZNU-2. A) Binding site I as a single C_3H_4 molecule trap. B) Binding site II inside the cage. C–E) 2, 6, and 10 C_3H_4 molecules adsorbed inside the cage.

beneficial for C_3H_4/C_3H_6 separation. Notably, the C_3H_4 uptake at 1 kPa on ZNU-2 is even higher than the uptakes of SIFSIX-3-Ni (2.98 mmol g^{-1}),[13] ELM-12 (2.74 mmol g^{-1}),[16] ZU-62 (3.66 mmol g^{-1}),[17] UTSA-200 (3.62 mmol g^{-1}),[12a] TIFSIX-14-Cu-i (3.88 mmol g^{-1}) and GeFSIX-14-Cu-i (3.36 mmol g^{-1})[18] at 100 kPa (Figure 2D). The C_3H_4 capacity at 10 kPa is increased to 6.18 mmol g^{-1}, higher than those of most MOFs in the context of C_3H_4/C_3H_6 separation but slightly lower than the benchmark of Cu-BTC (8.17 mmol g^{-1}) (Figure 2D).[12]

As separation selectivity is as important as the capacity, the C_3H_4/C_3H_6 selectivity on ZNU-2 at 298 K was calculated by using ideal adsorbed solution theory (IAST) after fitting isotherms to the dual-site Langmuir–Freundlich equation with excellent accuracy. Figure 2E revealed that the selectivity for 1/99 C_3H_4/C_3H_6 is 12.5, higher than those of ZIF-8 (1.9), Cu-BTC (3.2), MIL-100(Cr) (4.5), and SIFSIX-1-Cu (9.0) (Figure 2E).[12a,13] Increasing the ratio of C_3H_4 in the gas mixture leads to increased C_3H_4/C_3H_6 selectivity, which is 13.7 and 16.2 for 10/90 and 50/50 C_3H_4/C_3H_6 mixtures, respectively. The increase of the C_3H_4/C_3H_6 selectivity along with the uptakes or C_3H_4 ratios suggests the potential cooperative interactions inside ZNU-2. The static C_3H_4 and C_3H_6 uptakes from the 10/90 mixture of C_3H_4/C_3H_6 were calculated for ZNU-2 and other leading materials. The separation potential ($\Delta q = q_1y_2/y_1 - q_2$) as a combined selectivity-capacity metric firstly introduced by Krishna[19] for the evaluation of separation performance was utilized here for further comparison, which showed a trend of ZNU-2 (31.0 mmol g^{-1}) > SIFSIX-1-Cu (29.0 mmol g^{-1}) > TIFSIX-14-Ni-i (27.3 mmol g^{-1}) > GeFSIX-14-Ni-i (26.3 mmol g^{-1}) > SIFSIX-14-Ni-i (24.6 mmol g^{-1}) > SIFSIX-3-Ni (24.1 mmol g^{-1}) > SIFSIX-2-Cu-i (23.4 mmol g^{-1}) > ZU-62 (22.4 mmol g^{-1}) > NKMOF-11 (22.0 mmol g^{-1})[20] > ELM-12 (21.2 mmol g^{-1}) at 100 kPa and 298 K (Figure 2F). The C_3H_4 and C_3H_6 adsorption isotherms on ZNU-2 were further collected at 278 K and 308 K and all revealed type I isotherms (Figure 2B). The isosteric enthalpy of adsorption (Q_{st}) for ZNU-2 was then calculated using the Clausius–Clapeyron equation. Q_{st} values at near-zero loading for C_3H_4 and C_3H_6 were 43.0 and 34.5 kJ mol^{-1} (Figure 2G).

The Q_{st} value for C_3H_4 in ZNU-2 is lower than those of most MOFs for C_3H_4/C_3H_6 separation such as ZU-62 (71 kJ mol^{-1}), SIFSIX-3-Ni (68 kJ mol^{-1}), NKMOF-1-Ni (65.1 kJ mol^{-1}),[21] Ca-based MOF (55.4 kJ mol^{-1}),[22] UTSA-200 (55.3 kJ mol^{-1}), ELM-12 (60.6 kJ mol^{-1}) and SIFSIX-2-Cu-i (46 kJ mol^{-1}), but slightly higher than that of SIFSIX-1-Cu (37 kJ mol^{-1}). Such moderate Q_{st} endows the preferential C_3H_4 adsorption as well as facile recovery of C_3H_4 by desorption under mild conditions. To further compare the adsorption difference of C_3H_4 and C_3H_6 on ZNU-2, we studied the kinetic adsorption behavior. The adsorption rate of C_3H_4 in ZNU-2 is slightly faster than that of C_3H_6. The adsorption of C_3H_4 reached equilibrium within 15 mins while that for C_3H_6 was over 20 mins (Figure 2H). Such diffusion difference has not been reported in other fluorinated anion pillared porous MOFs with smooth one-dimensional channels. In brief, ZNU-2 is preferential for C_3H_4 adsorption in both thermodynamics and kinetics.

To gain more insight into the gas adsorption behavior, grand canonical Monte Carlo (GCMC) simulations were performed. Two different binding sites were observed: one located in the channel between two cages and the other inside the cage. Moreover, the results indicated that 25 C_3H_4 molecules can be adsorbed in single unit cell at 298 K and 100 kPa (Figure S37), equal to 7.49 mmol g^{-1} of C_3H_4 for ZNU-2, consistent with the experimental value of 7.7 mmol g^{-1}. DFT calculations were then applied to identify the adsorption configuration and binding energies of C_3H_4 in ZNU-2. Figure 3A showed that the C_3H_4 molecule in the first binding site is perpendicular to the channel between two cages. The three hydrogen atoms from the methyl group in C_3H_4 were strongly interacting with three F atoms at the edge of three different cages in the distances of 2.23, 2.77 and 2.79 Å besides additional multiple Van der waals interactions (Figure S28). The binding energy is 48.8 kJ mol^{-1}, close to the experimental Q_{st} (43.0 kJ mol^{-1}). Due to the contracted aperture and short length of channel, only one C_3H_4 can be accommodated, which could be regarded as a single C_3H_4 molecule trap for strong C_3H_4 adsorption. The second binding site locating inside the cage adsorbs C_3H_4 by two strong hydrogen bonds between the terminal hydrogen of C_3H_4 and two adjacent F atoms with distances of 2.07 and 2.57 Å (Figure 3B). This binding energy is 41.2 kJ mol^{-1}. Interestingly, the accommodation of C_3H_4 inside the cages is boosted by the adsorbed C_3H_4 molecules. The binding energy for the second C_3H_4 molecule inside the cage increases to 45.7 kJ mol^{-1}. Thus, the average binding energy of two C_3H_4 molecules inside the cavity is 43.4 kJ mol^{-1}, which increased to 44.9, 45.4, and 47.0 kJ mol^{-1} for accommodation of 5, 6 and 10 C_3H_4 molecules in a cage (Figure 3C–E, S29–S36). This rare boosted adsorption phenomenon results from the synergism of framework···C_3H_4 and C_3H_4···C_3H_4 interactions and is consistent with the IAST selectivity increase trend. Thus, combining single C_3H_4 molecule trap for tight C_3H_4 binding and large volume pores for accelerated C_3H_4 adsorption, ZNU-2 represents one of the best MOFs for C_3H_4 adsorption and storage.

To confirm the practical separation performance of ZNU-2 for selective C_3H_4/C_3H_6 separation, transient breakthrough simulations were conducted for 10:90 C_3H_4/C_3H_6 mixture. The results showed that highly efficient separations could be accomplished by ZNU-2 (Figure 4A). The productivity of C_3H_6 (>99.996 % purity) in a single adsorption process is also calculated for ZNU-2 and other benchmark materials, which showed ZNU-2 has the highest C_3H_6 productivity of 25.9 mol kg^{-1} (Figure 4B), consistent with the separation potential Δq_{IAST} based on the static gas adsorption isotherms. Experimental breakthrough studies with

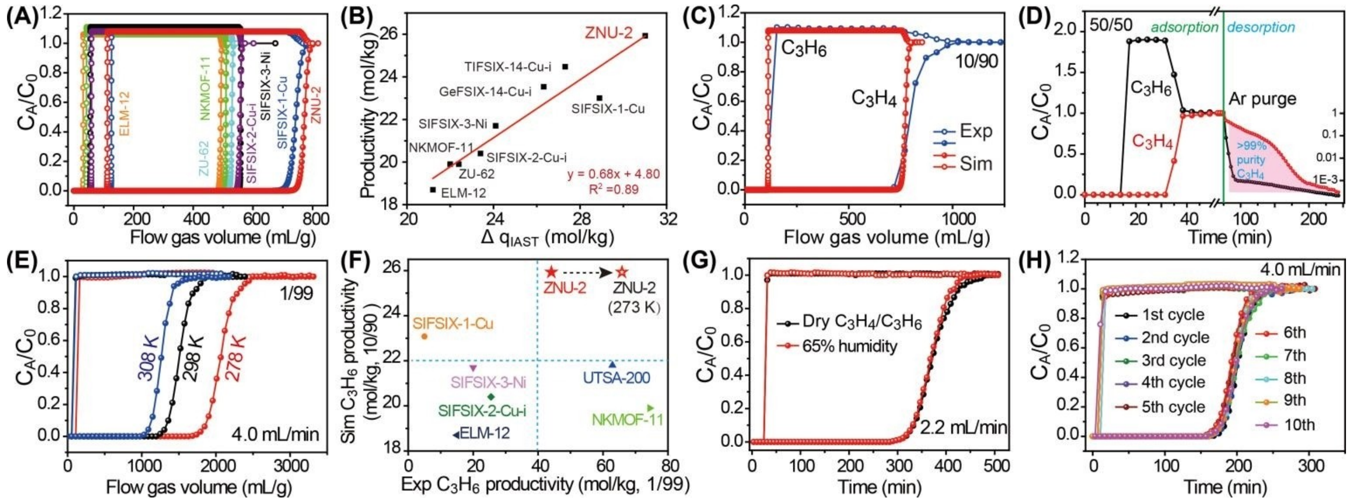

Figure 4. A) Simulated breakthrough curves of ZNU-2 and other top-performing materials for C_3H_4/C_3H_6 (10/90) at 298 K. B) Plots of the calculated productivity of C_3H_6 in >99.996 % purity and separation potential Δq_{IAST}. C) Comparison of the experimental and simulated breakthrough curves for C_3H_4/C_3H_6 (10/90). D) Experimental breakthrough curves and desorption curves of ZNU-2 for C_3H_4/C_3H_6 (50/50) at 298 K. E) Experimental breakthrough curves of ZNU-2 for C_3H_4/C_3H_6 (1/99) at 278, 298, and 308 K. F) Comparison of the C_3H_6 productivity from 10/90 and 1/99 C_3H_4/C_3H_6. G) Experimental breakthrough curves of ZNU-2 for C_3H_4/C_3H_6 (1/99) at 298 K under dry and humid conditions. H) Ten cycles of experimental breakthrough curves of ZNU-2 for C_3H_4/C_3H_6 (1/99) at 298 K.

C_3H_4/C_3H_6 (10/90) mixture flowed over a ZNU-2 packed column with a flow rate of 4 mL min^{-1} at 298 K was then carried out. The experimental results were highly close to the simulated one and 25.5 mol kg^{-1} of high purity C_3H_6 can be produced (Figure 4C). To thoroughly evaluate the separation performance of ZNU-2, we conducted more breakthrough experiments under various conditions. C_3H_4/C_3H_6 mixtures contain a higher ratio (50 %) or lower ratio (1 %) of C_3H_4 were tested. In both cases, clean separations were achieved. For 50:50 C_3H_4/C_3H_6 mixture, the retaining time of C_3H_4 is more than twice of that of C_3H_6. 5.8 mol kg^{-1} of C_3H_4 was captured in the column with a purity of $\approx$87 % (Figure 4D). Controlling the desorption conditions,[8a] 4.1 mol kg^{-1} of $>$99 % purity C_3H_4 can be recovered from the column by evacuation after blowing C_3H_6 out in the first stage (Figures 4D, S41). Such high dynamic productivity of C_3H_4 is impossible to be realized by other fluorinated anion pillared ultramicroporous materials because of their low C_3H_4 capacity. For 1:99 C_3H_4/C_3H_6 mixture, C_3H_6 broke out at $\approx$14 mins and got saturated immediately while C_3H_4 was detected until $\approx$168 mins and reached saturation slowly (Figure 4E). The calculated experimental productivity of C_3H_6 from 1:99 C_3H_4/C_3H_6 mixture is 42.0 mol kg^{-1}, much higher than those of SIFSIX-1-Cu (5 mol kg^{-1}), ELM-12 (15 mol kg^{-1}), SIFSIX-3-Ni (20 mol kg^{-1}) and SIFSIX-2-Cu-i (25.5 mol kg^{-1}), only lower than those of UTSA-200 (62.9 mol kg^{-1})[12a] and NKMOF-11 (74.4 mol kg^{-1}) (Figure 4F).[20] Decreasing the experimental temperature led to enhanced C_3H_6 productivity for ZNU-2 and the production value increased to ca. 67 mol kg^{-1} under 278 K. Due to its extremely high stability, we further conducted the breakthrough experiments under humid conditions. The C_3H_4/C_3H_6 mixture was firstly bubbled into a bottle full of water and then introduced into the column packed with ZNU-2. The humidity was measured constantly, which rose to $\approx$65 % after reaching equilibrium. The experimental results showed that the influence of moisture is negligible for C_3H_4/C_3H_6 separation in ZNU-2 (Figure 4G). Repetitive breakthrough experiments indicated the excellent separation capacity of ZNU-2 is retained over 10 cycles (Figure 4H). In brief, the combination of high productivity of polymer-grade C_3H_6, the large amount of C_3H_4 recovered, retaining separation performance under humid conditions, good recycling capacity and facile regeneration conditions renders ZNU-2 as one of the best adsorbents for practical C_3H_6 purification and C_3H_4 recovery/storage.

Conclusion

In conclusion, we reported an unprecedented ultrastable fluorinated anion cross-linked cage-like metal–organic framework for simultaneous benchmark propyne recovery and propylene purification by comprehensively tuning the pore size, shape and functionality. The combination of large C_3H_4 capacity (3.9/7.7 mmol g^{-1} at 0.01/1.0 bar and 298 K), high C_3H_4/C_3H_6 selectivity (12.5–16.2), low adsorption enthalpy (43.0 kJ mol^{-1}) for regeneration as well as ultrahigh stability has been realized for the first time. The efficient separation of mixed C_3H_4/C_3H_6 gases was practically confirmed by column-breakthrough experiments under various conditions with good recyclability. 25.5 and 42.0 mol kg^{-1} of $>$99.996 % purity C_3H_6 can be produced from 10/90 and 1/99 C_3H_4/C_3H_6 mixtures, respectively. 4.1 mol kg^{-1} of 99 % purity C_3H_4 can be recovered by stepped desorption from the column for 50/50 C_3H_4/C_3H_6 mixtures. Modeling studies indicated efficient C_3H_4 adsorption was realized by cooperative single C_3H_4 molecule trap and boosted C_3H_4 adsorption binding sites. In general, our work demonstrates the significance of the comprehensive pore tuning in porous materials to construct multiple cooperative functional sites for gas separation and storage.

Acknowledgements

This work was supported by the National Natural Science Foundation of China (No. 21908193, 21938011, 22008209, 21871231), and the Research Computing Center in College of Chemical and Biological Engineering at Zhejiang University.

Conflict of Interest

The authors declare no conflict of interest.

Data Availability Statement

The data that support the findings of this study are available from the corresponding author upon reasonable request.

Keywords: C_3H_4 Storage · C_3H_4/C_3H_6 Separation · Cooperative Interactions · Metal–Organic Frameworks · Pore Tuning

---

[1] a) I. Amghizar, L. A. Vandewalle, K. M. Van Geem, G. B. Marin, *Engineering* **2017**, *3*, 171–178; b) M.-Y. Gao, B.-Q. Song, D. Sensharma, M. J. Zaworotko, *SmartMat* **2021**, *2*, 38–55.

[2] A. Chavel, G. Lefebvre, *Petrochemical Process, Institut Francais du Petrole Publications*, Gulf Publishing, **1989**, pp. 199–208.

[3] a) Z. Miao, A. M. Esper, S. S. Nadif, S. A. Gonsales, B. S. Sumerlin, A. S. Veige, *React. Funct. Polym.* **2021**, *169*, 105088; b) J. L. Alterman, G. A. Kraus, *Synthesis* **2021**, *54*, 655–657.

[4] a) C. He, R. Krishna, Y. Chen, J. Yang, J. Li, L. Li, *Chin. J. Chem. Eng.* **2021**, *37*, 217–221; b) Y. Chai, X. Han, W. Li, S. Liu, S. Yao, C. Wang, W. Shi, I. Da-Silva, P. Manuel, Y. Cheng, L. D. Daemen, A. J. Ramirez-Cuesta, C. C. Tang, L. Jiang, S. Yang, N. Guan, L. Li, *Science* **2020**, *368*, 1002–1006.

[5] a) H. Wang, J. Li, *Acc. Chem. Res.* **2019**, *52*, 1968–1978; b) B. R. Barnett, M. I. Gonzalez, J. R. Long, *Trends Chem.* **2019**, *1*, 159–171; c) X. Zhao, Y. Wang, D. S. Li, X. Bu, P. Feng, *Adv. Mater.* **2018**, *30*, 1705189; d) R.-B. Lin, S. Xiang, W. Zhou, B. Chen, *Chem* **2020**, *6*, 337–363; e) T. Ke, Q. Wang, J. Shen, J. Zhou, Z. Bao, Q. Yang, Q. Ren, *Angew. Chem. Int. Ed.* **2020**, *59*, 12725–12730; *Angew. Chem.* **2020**, *132*, 12825–12830.

[6] a) Z. Shi, Y. Tao, J. Wu, C. Zhang, H. He, L. Long, Y. Lee, T. Li, Y. Zhang, *J. Am. Chem. Soc.* **2020**, *142*, 2750–2754; b) S. Edubilli, S. Gumma, *Sep. Purif. Technol.* **2019**, *224*, 85–94; c) C. Yu, Q. Ding, J. Hu, Q. Wang, X. Cui, H. Xing, *Chem. Eng. J.* **2021**, *405*, 126937; d) O. T. Qazvini, S. G. Telfer, *ACS Appl. Mater. Interfaces* **2021**, *13*, 12141–12148.

[7] a) K. Chen, D. G. Madden, T. Pham, K. A. Forrest, A. Kumar, Q. Yang, W. Xue, B. Space, J. J. Perry IV, J. Zhang, X. Chen, M. J. Zaworotko, *Angew. Chem. Int. Ed.* **2016**, *55*, 10268–10272; *Angew. Chem.* **2016**, *128*, 10424–10428; b) S. C. King, R. Lin, H. Wang, H. D. Arman, B. Chen, *Mater. Chem. Front.* **2017**, *1*, 1514–1519; c) R. L. Siegelman, P. J. Milner, A. C. Forse, J. Lee, K. A. Colwell, J. B. Neaton, J. A. Reimer, S. C. Weston, J. R. Long, *J. Am. Chem. Soc.* **2019**, *141*, 13171–13186.

[8] a) L. Wang, W. Sun, Y. Zhang, N. Xu, R. Krishna, J. Hu, Y. Jiang, Y. He, H. Xing, *Angew. Chem. Int. Ed.* **2021**, *60*, 22865–22870; *Angew. Chem.* **2021**, *133*, 23047–23052; b) H. Zeng, M. Xie, Y.-L. Huang, Y. Zhao, X.-J. Xie, J. -Bai, M.-Y. Wan, R. Krishna, W. Lu, D. Li, *Angew. Chem. Int. Ed.* **2019**, *58*, 8515–8519; *Angew. Chem.* **2019**, *131*, 8603–8607; c) L. Yang, L. Yan, Y. Wang, Z. Liu, J. He, Q. Fu, D. Liu, X. Gu, P. Dai, L. Li, X. Zhao, *Angew. Chem. Int. Ed.* **2021**, *60*, 4570–4574; *Angew. Chem.* **2021**, *133*, 4620–4624; d) Z. Niu, X. Cui, T. Pham, G. Verma, P. C. Lan, C. Shan, H. Xing, K. A. Forrest, S. Suepaul, B. Space, A. Nafady, A. M. Al-Enizi, S. Ma, *Angew. Chem. Int. Ed.* **2021**, *60*, 5283–5288; *Angew. Chem.* **2021**, *133*, 5343–5348; e) H. Li, C. Liu, C. Chen, Z. Di, D. Yuan, J. Pang, W. Wei, M. Wu, M. Hong, *Angew. Chem. Int. Ed.* **2021**, *60*, 7547–7552; *Angew. Chem.* **2021**, *133*, 7625–7630.

[9] a) Y. Zhang, J. Hu, R. Krishna, L. Wang, L. Yang, X. Cui, S. Duttwyler, H. Xing, *Angew. Chem. Int. Ed.* **2020**, *59*, 17664–17669; *Angew. Chem.* **2020**, *132*, 17817–17822; b) R.-B. Lin, L. Li, H. Wu, H. Arman, B. Li, R.-G. Lin, W. Zhou, B. Chen, *J. Am. Chem. Soc.* **2017**, *139*, 8022–8028; c) X. Cui, K. Chen, H. Xing, Q. Yang, R. Krishna, Z. Bao, H. Wu, W. Zhou, X. Dong, Y. Han, B. Li, Q. Ren, M. J. Zaworotko, B. Chen, *Science* **2016**, *353*, 141–144; d) Y.-L. Peng, T. Pham, P. Li, T. Wang, Y. Chen, K.-J. Chen, K. A. Forrest, B. Space, P. Cheng, M. J. Zaworotko, Z. Zhang, *Angew. Chem. Int. Ed.* **2018**, *57*, 10971–10975; *Angew. Chem.* **2018**, *130*, 11137–11141.

[10] a) Q. Ding, Z. Zhang, C. Yu, P. Zhang, J. Wang, X. Cui, C.-H. He, S. Deng, H. Xing, *Sci. Adv.* **2020**, *6*, eaaz4322; b) A. A. Lysova, D. G. Samsonenko, K. A. Kovalenko, A. S. Nizovtsev, D. N. Dybtsev, V. P. Fedin, *Angew. Chem. Int. Ed.* **2020**, *59*, 20561–20567; *Angew. Chem.* **2020**, *132*, 20742–20748; c) L. Li, R. Lin, R. Krishna, H. Li, S. Xiang, H. Wu, J. Li, W. Zhou, B. Chen, *Science* **2018**, *362*, 443–446; d) D. Lv, P. Zhou, J. Xu, S. Tu, F. Xu, J. Yan, H. Xi, W. Yuan, Q. Fu, X. Chen, Q. Xia, *Chem. Eng. J.* **2022**, *431*, 133208.

[11] a) H. Li, L. Li, R.-B. Lin, W. Zhou, Z. Zhang, S. Xiang, B. Chen, *EnergyChem* **2019**, *1*, 100006; b) K. Adil, Y. Belmabkhout, R. S. Pillai, A. Cadiau, P. M. Bhatt, A. H. Assen, G. Maurin, M. Eddaoudi, *Chem. Soc. Rev.* **2017**, *46*, 3402–3430; c) L. Yang, S. Qian, X. Wang, X. Cui, B. Chen, H. Xing, *Chem. Soc. Rev.* **2020**, *49*, 5359–5406.

[12] a) L. Li, H. Wen, C. He, R. Lin, R. Krishna, H. Wu, W. Zhou, J. Li, B. Li, B. Chen, *Angew. Chem. Int. Ed.* **2018**, *57*, 15183–15188; *Angew. Chem.* **2018**, *130*, 15403–15408; b) Y. Peng, T. Wang, C. Jin, C. Deng, Y. Zhao, W. Liu, K. A. Forrest, R. Krishna, Y. Chen, T. Pham, B. Space, P. Cheng, M. J. Zaworotko, Z. Zhang, *Nat. Commun.* **2021**, *12*, 5768.

[13] L. Yang, X. Cui, Q. Yang, S. Qian, H. Wu, Z. Bao, Z. Zhang, Q. Ren, B. Chen, H. Xing, *Adv. Mater.* **2018**, *30*, 1705374.

[14] a) L. Yang, X. Cui, Y. Zhang, Q. Wang, Z. Zhang, X. Suo, H. Xing, *ACS Sustainable Chem. Eng.* **2019**, *7*, 3138–3144; b) L. Yang, A. Jin, L. Ge, X. Cui, H. Xing, *Chem. Commun.* **2019**, *55*, 5001–5004.

[15] M. Lusi, P. B. A. Fechine, K.-J. Chen, J. J. Perry IV, M. J. Zaworotko, *Chem. Commun.* **2016**, *52*, 4160–4162.

[16] L. Li, R.-L. Lin, R. Krishna, X. Wang, B. Li, H. Wu, J. Li, W. Zhou, B. Chen, *J. Am. Chem. Soc.* **2017**, *139*, 7733–7736.

[17] L. Yang, X. Cui, Z. Zhang, Q. Yang, Z. Bao, Q. Ren, H. Xing, *Angew. Chem. Int. Ed.* **2018**, *57*, 13145–13149; *Angew. Chem.* **2018**, *130*, 13329–13333.

[18] L. Yang, X. Cui, Y. Zhang, Q. Yang, H. Xing, *J. Mater. Chem. A* **2018**, *6*, 24452–24458.

[19] a) R. Krishna, *RSC Adv.* **2017**, *7*, 35724–35737; b) R. Krishna, *Sep. Purif. Technol.* **2018**, *194*, 281–300; c) R. Krishna, *ACS Omega* **2020**, *5*, 16987–17004.

[20] Y. Peng, T. Wang, C. Jin, P. Li, S. Suepaul, G. Beemer, Y. Chen, R. Krishna, P. Cheng, T. Pham, B. Space, M. J. Zaworotko, Z. Zhang, *J. Mater. Chem. A* **2021**, *9*, 2850–2856.

[21] Y. Peng, C. He, T. Pham, T. Wang, P. Li, R. Krishna, K. A. Forrest, A. Hogan, S. Suepaul, B. Space, M. Fang, Y. Chen, M. J. Zaworotko, J. Li, L. Li, Z. Zhang, P. Cheng, B. Chen, *Angew. Chem. Int. Ed.* **2019**, *58*, 10209–10214; *Angew. Chem.* **2019**, *131*, 10315–10320.

[22] L. Li, L. Guo, F. Zhang, Z. Zhang, Q. Yang, Y. Yang, Q. Ren, Z. Bao, *ACS Appl. Mater. Interfaces* **2020**, *12*, 17147–17154.

[23] Deposition Number 2142633 (for ZNU-2) contains the supplementary crystallographic data for this paper. These data are provided free of charge by the joint Cambridge Crystallographic Data Centre and Fachinformationszentrum Karlsruhe Access Structures service.

Manuscript received: January 18, 2022
Accepted manuscript online: February 24, 2022
Version of record online: March 7, 2022

Angewandte Chemie
Eine Zeitschrift der Gesellschaft Deutscher Chemiker

Supporting Information

Comprehensive Pore Tuning in an Ultrastable Fluorinated Anion Cross-Linked Cage-Like MOF for Simultaneous Benchmark Propyne Recovery and Propylene Purification

*Y. Jiang, J. Hu, L. Wang, W. Sun, N. Xu, R. Krishna, S. Duttwyler, X. Cui, H. Xing, Y. Zhang**

I General Information and Procedures

Unless otherwise noted, all the reactions were performed under air without N_2 or Ar protection. All reagents were used as received without purification unless stated otherwise.

Chemicals: Tri(pyridin-4-yl)amine (TPA, 99%) was purchased from Tensus Biotech Company. 4,4’-Bipyridine (98%) and pyrazine (99%) were purchased from Energy Chemical. 1,2-Di(pyridin-4-yl)ethyne (97%) and 1,2-di(pyridin-4-yl)diazene (98%) wee purchased from Chemsoon. The purity of all organic compounds was identified by ^1H NMR and $^{13}C\{^1H\}$ NMR. $Cu[NO_3]_2{\cdot}3H_2O$ (99%), $Ni(BF_4)_2$ (99%) and $(NH_4)_2GeF_6$ (99.99%) were purchased from Energy Chemical. $(NH_4)_2TiF_6$ (98%) was purchased from Alab Chemical. C_3H_4 (99.9%), C_3H_6 (99.9%), N_2(99.9999%), He (99.9999%), Ar (99.9999%), C_3H_4/C_3H_4 (50:50), C_3H_4/C_3H_4 (10:90) and C_3H_4/C_3H_4 (1:99) were purchased from Datong Co., Ltd. All other reagents were purchased from Adamas-beta and used without further purification.

Preparation of ZNU-2: To a 5 mL long thin tube was added a 1 mL of aqueous solution with $Cu(NO_3)_2{\cdot}3H_2O$ (~1.3 mg) and $(NH_4)_2TiF_6$ (~1.0 mg). 2 mL of $MeOH/H_2O$ mixture (v:v=1:1) was slowly layered above the solution, followed by a 1 mL of MeOH solution of TPA (~1.0 mg). The tube was sealed and left undisturbed at 298 K. After ~1 week, purple single crystals were obtained.

Preparation of SIFSIX-1-Cu: SIFSIX-1-Cu was prepared according to the reported literature.[1-3] 58.3 mg 4,4’-bipyridine (0.37 mmol) was dissolved in 6.5 mL ethylene glycol at 338 K in a 25 mL round bottom flask and an aqueous solution (3 mL) of $CuSiF_6{\cdot}4H_2O$ (51.8 mg, 0.19 mmol) was added to the former solution. The mixture was then heated at 338K for 3 h with stirring. The obtained purple powder was washed with methanol, and soaked in anhydrous MeOH for storage.

Preparation of of SIFSIX-2-Cu-i: SIFSIX-2-Cu-i was prepared according to the reported literature.[2-4] A MeOH solution (4.0 mL) of 1,2-di(pyridin-4-yl)ethyne (~51.5 mg, 0.286 mmol) was mixed with an aqueous solution (4.0 mL) of $CuSiF_6·4H_2O$ (~72.2 mg, 0.260 mmol) in a 25 mL round bottom flask and then heated at 358 K for 12 h. The obtained blue powder was washed with methanol, and soaked in anhydrous MeOH for storage. Single crystals of SIFSIX-2-Cu-i was prepared according to the reported literature[4]: To a 5 mL long thin tube was added 2 mL of DMSO solution of 1,2-di(pyridin-4-yl)ethyne (20.7 mg). 2 mL of MeOH solution of $CuSiF_6·4H_2O$ (41.4 mg) was slowly layered above the solution. The tube was sealed and left undisturbed at 298 K. After ~1 week, blue single crystals were obtained.

Preparation of ZU-62: ZU-62 was prepared according to the reported literature.[5] A preheated water solution (4.0 mL) of $CuNbOF_5$ (~73.0 mg) was mixed with a preheated methanol solution (4.0 mL) of 1,2-di(pyridin-4-yl)ethyne (~51.5 mg) in a 25 mL round bottom flask. Then the mixture was heated at 353 K for 24 h. The obtained blue powder was washed with methanol, and soaked in anhydrous MeOH for storage. Single crystals of ZU-62 were prepared according to the reported literature[5]: To a long thin tube was added 3 mL of DMSO solution with 1,2-di(pyridin-4-yl)ethyne (~21.9 mg). 2 mL of DMSO/MeOH mixture (v:v=1:1) was slowly layered above the solution, followed by 3 mL of MeOH solution of $CuNbOF_5$ (~15 mg). The tube was sealed and left undisturbed at 298 K. After ~1 week, blue single crystals were obtained.

Prparation of SIFSIX-3-Ni: SIFSIX-3-Ni was prepared according to the reported literature.[2-3,6] A methanol solution (20 mL) of $(NH_4)_2SiF_6$ (1 mmol)， $Ni(BF_4)_2$ (1 mmol) and pyrazine (2 mmol) was mixed in a 50 mL round bottom flask, and then heated at 358 K for 3 days. The obtained blue powder was washed with methanol/water, and soaked in anhydrous MeOH for storage.

Preparation of SIFSIX-14-Cu-i: SIFSIX-14-Cu-i was prepared according to the reported literature.[7-8] A methanol solution (3.0 mL) of 1,2-di(pyridin-4-yl) diazene (~49.0 mg) was mixed with an aqueous solution (2.5 mL) of $CuSiF_6$ (~68.6 mg) in a 25 mL round bottom flask. Then the mixture was heated at 353 K for 15 min, additional 1 h at 323 K, and then at 298 K for 24 h resulting in a bright grey precipitate, which was then washed with methanol, and soaked in anhydrous MeOH for storage. Single crystals of SIFSIX-14-Cu-i were prepared according to the reported literature[7]: Saffron prism-shaped single crystals of SIFSIX-14-Cu-i/UTSA-200 were synthesized in quantitative yield at room temperature by slow diffusion of a methanol solution of $CuSiF_6$ (2 mL, 0.15 mmol) into a DMSO solution of 1,2-di(pyridin-4-yl)diazene (0.12 mmol) after one week.

Preparation of TIFSIX-14-Cu-i: TIFSIX-14-Cu-i was prepared according to the reported literature.[9] A preheated ethanol solution (2.0 mL) of 1,2-di(pyridin-4-yl)diazene (~60.0 mg) was mixed with a preheated glycol solution (3.0 mL) of $Cu(NO_3)_2{\cdot}3H_2O$ (~60.4 mg) and $(NH_4)_2TiF_6$ (~49.5 mg) in a 25 mL round bottom flask. Then the mixture was heated at 338 K for 24 h. The obtained brownish red powder was washed with methanol, and soaked in anhydrous MeOH for storage. Single crystals of TIFSIX-14-Cu-i were prepared according to the reported literature[9]: To a long thin tube was added 3 mL of DMSO solution with 1,2-di(pyridin-4-yl)diazene (~9 mg). 1 mL of DMSO/ MeOH mixture (v:v=1:1) was slowly layered above the solution, followed by 3 mL of MeOH solution of $Cu(NO_3)_2{\cdot}3H_2O$ (~9.1 mg) and $(NH_4)_2TiF_6$ (~7.5 mg). The tube was sealed and left undisturbed at 298 K. After ~1 week, blue single crystals were obtained.

Preparation of GeFSIX-14-Cu-i: GeFSIX-14-Cu-i was prepared according to the reported literature.[10] A methanol solution (20.0 mL) of 1,2-di(pyridin-4-yl)diazene (~50.3 mg) was mixed with an aqueous solution (25.0 mL) of $Cu(NO_3)_2{\cdot}3H_2O$ (~62.8 mg) and $(NH_4)_2GeF_6$ (~57.9 mg) in a 100 mL round bottom flask. Then the mixture was heated at 298 K for 24 h. The obtained brownish red powder was washed with methanol, and soaked in anhydrous MeOH for storage. Single crystals of GeFSIX-14-Cu-i were prepared according to the reported literature[10]: To a long thin tube was added 3 mL of DMSO solution with 1,2-di(pyridin-4-yl)diazene (~9 mg). 1 mL of DMSO/ MeOH mixture (v:v=1:1) was slowly layered above the solution, followed by 3 mL of MeOH solution of $Cu(NO_3)_2 \cdot 3H_2O$ (~9.1 mg) and $(NH_4)_2GeF_6$ (~8.4 mg). The tube was sealed and left undisturbed at 298 K. After ~2 week, blue single crystals were obtained.

[1] S. Noro, R. Kitaura, M. Kondo, S. Kitagawa, T. Ishii, H. Matsuzaka, M. Yamashita, *J. Am. Chem. Soc.* **2002**, *124*, 2568–2583.

[2] X. Cui, K. Chen, H. Xing, Q. Yang, R. Krishna, Z. Bao, H. Wu, W. Zhou, X. Dong, Y. Han, B. Li, Q. Ren, M. J. Zaworotko, B. Chen, *Science* **2016**, *353*, 141-144.

[3] L. Yang, X. Cui, Q. Yang, S. Qian, H. Wu, Z. Bao, Z. Zhang, Q. Ren, W. Zhou, B. Chen, H. Xing, *Adv. Mater.* **2018**, *30,* 1705374.

[4] P. Nugent, Y. Belmabkhout, S. D. Burd, A. J. Cairns, R. Luebke, K. Forrest, T. Pham, S. Ma, B. Space, L. Wojtas, M. Eddaoudi, M. J. Zaworotko, *Nature* **2013**, *495*, 80-84.

[5] L. Yang, X. Cui, Z. Zhang, Q. Yang, Z. Bao, Q. Ren, H. Xing, *Angew. Chem. Int. Ed.* **2018**, *57*, 13145-13149.

[6] A. Kumar, D. G. Madden, M. Lusi, K. J. Chen, E. A. Daniels, T. Curtin, J. J. t. Perry, M. J. Zaworotko, *Angew. Chem. Int. Ed.* **2015**, *54*, 14372-14377.

[7] B. Li, X. Cui, D. O'Nolan, H. M. Wen, M. Jiang, R. Krishna, H. Wu, R. B. Lin, Y. S. Chen, D. Yuan, H. Xing, W. Zhou, Q. Ren, G. Qian, M. J. Zaworotko, B. Chen, *Adv. Mater.* **2017**, *29*, 1704210.

[8] L. Li, H. M. Wen, C. He, R. B. Lin, R. Krishna, H. Wu, W. Zhou, J. Li, B. Li, B. Chen, *Angew. Chem. Int. Ed.* **2018**, *57*, 15183-15188.

[9] L. Yang, X. Cui, Y. Zhang, Q. Yang, H. Xing, *J. Mater. Chem. A* **2018**, *6*, 24452-24458.

[10] Z. Zhang, Q. Yang, X. Cui, L. Yang, Z. Bao, Q. Ren, H. Xing, *Angew. Chem. Int. Ed.* **2017**, *56*, 16282-16287.

Single-crystal X-ray diffraction studies were conducted at 193 K on the BrukerAXS D8 VENTURE diffractometer equipped with a PHOTON-100/CMOS detector (GaKα, λ = 1.34139 Å). Indexing was performed using APEX2. Data integration and reduction were completed using SaintPlus 6.01. Absorption correction was performed by the multi-scan method implemented in SADABS. The space group was determined using XPREP implemented in APEX2.1 The structure was solved with SHELXS-97 (direct methods) and refined on F2 (nonlinear least-squares method) with SHELXL-97 contained in APEX2, WinGX v1.70.01, and OLEX2 v1.1.5 program packages. All non-hydrogen atoms were refined anisotropically. The contribution of disordered solvent molecules was treated as diffuse using the Squeeze routine implemented in Platon.

Powder X-ray diffraction (PXRD) data were collected on the SHIMADZU XRD-6000 diffractometer (Cu Kαλ = 1.540598 Å) with an operating power of 40 KV, 30 mA and a scan speed of 4.0°/min. The range of 2θ was from 5° to 50°.

Thermal gravimetric analysis was performed on the TGA STA449F5 instrument. Experiments were carried out using a platinum pan under nitrogen atmosphere which conducted by a flow rate of 60 mL/min nitrogen gas. First, the sample was heated at 80 °C for 1 h to remove the water residue and equilibrated for 5 minutes, then cooled down to 50 °C. The data were collected at the temperature range of 50 °C to 600 °C with a ramp of 10 °C /min.

The static gas adsorption equilibrium measurements were performed on the Builder SSA 7000 (Beijing) instrument. Before gas adsorption measurements, the sample of ZNU-2 (~100 mg) was evacuated at 25 ºC for 2 h firstly, and then at 120 ºC for 10 h until the pressure dropped below 7 μmHg. The sorption isotherms were collected at 77 K, 278, 298 and 308 K on activated samples.The experimental temperatures were controlled by liquid nitrogen bath (77 K), ethanol-water bath (273 K) and water bath (298 and 308 K), respectively.

Before gas adsorption measurements, the sample of SIFSIX-1-Cu was evacuated at 25 ºC for 24-48 h until the pressure dropped below 7 μmHg; the sample of SIFSIX-2-Cu-i was evacuated at 80 ºC for 2 days until the pressure dropped below 7 μmHg; the sample of ZU-62 was evacuated at 80 ºC for 2 days until the pressure dropped below 7 μmHg; the sample of SIFSIX-3-Ni was evacuated at 80 ºC for 2 days until the pressure dropped below 7 μmHg; the sample of SIFSIX-14-Cu-i was evacuated at 25 ºC for 36 h until the pressure dropped below 7 μmHg; the sample of TIFSIX-14-Cu-i was evacuated at 65 ºC for 24 h until the pressure dropped below 7 μmHg; the sample of GeFSIX-14-Cu-i was evacuated at 25 ºC for 18 h until the pressure dropped below 7 μmHg. The sorption isotherms were collected at 298 K on activated samples.

The gas adsorption kinetics measurements were performed on the TGA STA449F5 instrument. Before gas adsorption measurements, the sample of ZNU-2 was activated. After loading the activated ZNU-2 (3-5 mg) into the pan of the balance (precision: 10^{-7} g), it was firstly heated under N_2 flow (20 mL/min) from 25-150 °C with a ramp of 10 °C /min. The temperature of 150 °C was stayed for 1 hour. These steps were in order to remove the potential moisture adsorbed by the sample during the transfer of the sample into the instrument. Then, the sample was cooled to 25 °C under N_2 flow (20 mL/min). The temperature of 25 °C was stayed for 2 hours. Finally, C_3H_4, C_3H_6, or N_2 saturated with water vapor was introduced with a flow rate of 10 mL/min. The weight was measured constantly.

Fitting of experimental data on pure component isotherms

The unary isotherm data for C_3H_4, and C_3H_6, measured at three different temperatures 278 K, 298 K, and 308 K in ZNU-2 were fitted with good accuracy using the dual-site Langmuir-Freundlich model, where we distinguish two distinct adsorption sites A and B:

$$q = \frac{q_{sat,A} b_A p^{vA}}{1 + b_A p^{vA}} + \frac{q_{sat,B} b_B p^{vB}}{1 + b_B p^{vB}} \tag{S1}$$

Here, P is the pressure of the bulk gas at equilibrium with the adsorbed phase (Pa), q is the adsorbed amount per mass of adsorbent (mol kg^{-1}), $q_{sat,\ A}$ an $q_{sat,\ B}$ are the saturation capacities of site A and B (mol kg^{-1}), b_A and b_B are the affinity coefficients of site A and B (Pa^{-1}).

In eq (S1), the Langmuir-Freundlich parameters b_A, b_B can be temperature dependent or temperature independent .

$$b_A = b_{A0} \exp\left(\frac{E_A}{RT}\right); \quad b_b = b_{B0} \exp\left(\frac{E_B}{RT}\right) \tag{S2}$$

In eq (S2), E_A, E_B are the energy parameters associated with sites A, and B, respectively.

The isosteric heat of adsorption, Q_{st}, is defined as

$$Q_{st} = -RT^2 \left(\frac{\partial \ln p}{\partial T}\right)_q \tag{S3}$$

where the derivative in the right member of eq (S3) is determined at constant adsorbate loading, q. The calculations are based on the use of the Clausius-Clapeyron equation.

IAST calculations of adsorption selectivity and uptake capacities:

We consider the separation of binary 50/50 C_3H_4(1)/C_3H_6(2), 10/90 C_3H_4(1)/C_3H_6(2) and 1/99 C_3H_4(1)/C_3H_6(2) mixtures in various MOFs at 298 K, and varying total pressures.

The adsorption selectivity for separation of binary mixtures of species 1 and 2 is defined by

$$S_{ads} = \frac{q_1/q_2}{p_1/p_2} \tag{S4}$$

where q_1, q_2 are the molar loadings (units: mol kg^{-1}) in the adsorbed phase in equilibrium with a gas mixture with partial pressures p_1, p_2 in the bulk gas.

The C_3H_4(1)/C_3H_6(2) mixture separations are envisaged to be carried out in fixed bed adsorbers. In such devices, the separations are dictated by a combination of adsorption selectivity and uptake capacity. Using the shock wave model for fixed bed adsorbers, Krishna[1, 2] has suggested that the appropriate metric is the separation potential, Δq_2. The appropriate expression describing the productivity of pure C_3H_6 in the desorption phase of fixed-bed operations is

$$\Delta q_2 = q_1 \frac{y_{20}}{y_{10}} - q_2 \tag{S5}$$

In eq (S5) y_{10}, y_{20} are the mole fractions of the feed mixture during the adsorption cycle. In the derivation of eq (S5), it is assumed that the concentration “fronts” traversed the column in the form of shock waves during the desorption cycle. The Adsorbed Solution Theory (IAST) of Myers and Prausnitz using the unary isotherm fits as data inputs.[3] The physical significance of Δq_1 is the maximum productivity of pure C_3H_6(2) that is achievable in PSA operations.

Transient breakthrough simulations

The performance of industrial fixed bed adsorbers is dictated by a combination of adsorption selectivity and uptake capacity. Transient breakthrough simulations were carried out for 1/99 C_3H_4(1)/C_3H_6(2) mixtures operating at a total pressure of 100 kPa and 298 K, using the methodology described in earlier publications.[2] In these simulations, intra-crystalline diffusion influences are ignored.

For comparing the separation performance of MOFs, we carried out simulations of transient desorption in which we choose: length of packed bed, $L = 0.3$ m; superficial gas velocity at the entrance to the bed, $u_0 = 0.04$ m s^{-1}; voidage of the packed bed, ε = 0.4. We choose the mass of the adsorbent in the bed $m_{ads} = 180$ kg, cross-sectional area, $A = 1$ m^2; superficial gas velocity at the bed inlet, $u_0 = 0.04$ m s^{-1}; voidage of the packed bed, = 0.4. The interstitial gas velocity $v = \frac{u}{\varepsilon}$. If the total length of the bed is L m, the total volume of the bed is $V_{bed} = LA$. The volume of zeolite or MOF used in the simulations is $V_{ads} = LA(1-\varepsilon)$. It is important to note that the volume of adsorbent, V_{ads}, includes the pore volume of the adsorbent material. If ρ is the framework density, the mass of the adsorbent in the bed is $m_{ads} = (1-\varepsilon) \times (L \text{ m}) \times (A \text{ m}^2) \times (\rho \text{ kg m}^{-3})$ kg.

For presenting the breakthrough simulation results, we may use the dimensionless time, $\tau = \frac{tu}{L\varepsilon}$, obtained by dividing the actual time, t, by the characteristic time, $\frac{L}{v} = \frac{\varepsilon L}{u_0}$, where L is the length of adsorber, v is the interstitial gas velocity.

For comparison of breakthrough simulations with breakthrough experiments, it is most convenient to use $\frac{Q_0 t}{m_{ads}}$ as the x-axis when presenting the breakthrough simulation data

$$\frac{\left(Q_0 = \text{flow rate mL min}^{-1} \text{ at STP}\right) \times \left(\text{time in min}\right)}{\left(\text{g MOF packed in tube}\right)} = \frac{Q_0 t}{m_{ads}} = \text{mL g}^{-1} \tag{S6}$$

[1] R. Krishna, Screening Metal-Organic Frameworks for Mixture Separations in Fixed-Bed Adsorbers using a Combined Selectivity/Capacity Metric. *RSC Adv*. **2017**, *7*, 35724−35737.

[2] R. Krishna, Metrics for Evaluation and Screening of Metal-Organic Frameworks for Applications in Mixture Separations. *ACS Omega* **2020**, *5*, 16987−17004.

[3] A. L. Myers, J. M. Prausnitz, Thermodynamics of Mixed Gas Adsorption. *A.I.Ch.E.J. 1965*, **11**, 121−130.

Breakthrough experiments

The breakthrough experiments were carried out in the dynamic gas breakthrough equipment HP-MC41. The experiments were conducted using a stainless steel column (4.9 mm inner diameter × 100 length). The weight of ZNU-2 packed in the columns was 0.51 g. The column packed with sample was first purged with a Ar flow (5 mL min^{-1}) for 18 h at 120 °C. The mixed gas of C_3H_4/C_3H_6 (v/v,50:50, 10:90, 1:99) was then introduced. Outlet gas from the column was monitored using gas chromatography (GC-9860-5CNJ) with the thermal conductivity detector TCD. After the breakthrough experiment, the sample was regenerated with a Ar flow of 5 mL min^{-1} under 120 °C for 5 h.

The illustration of the gas breakthrough equipment working mechanism is showing as below: A-B) under work; C) under purge; D) under vacuum.

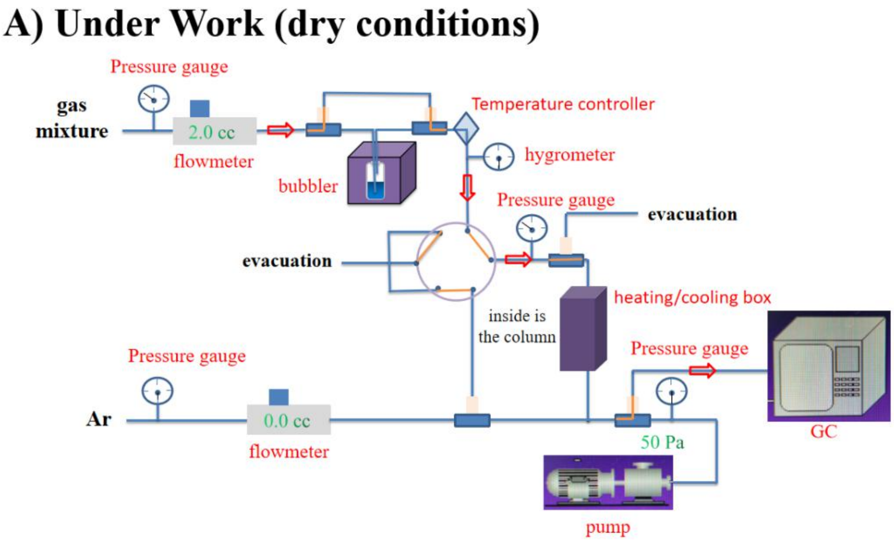

B) Under Work (humid conditions)

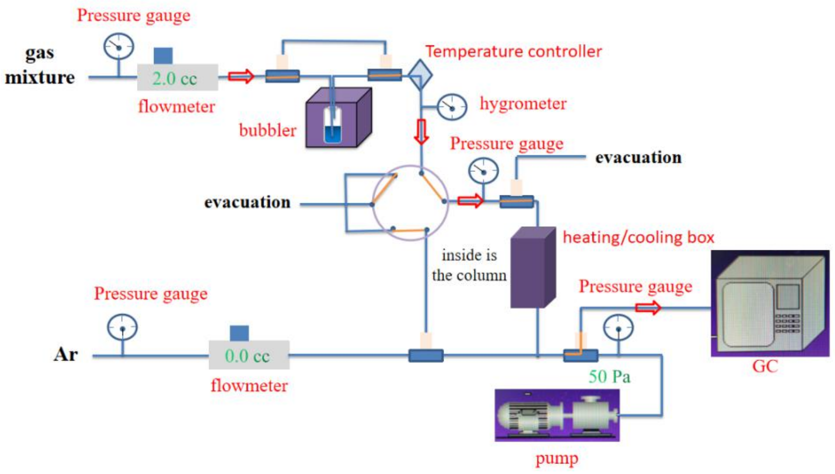

C) Under Purge

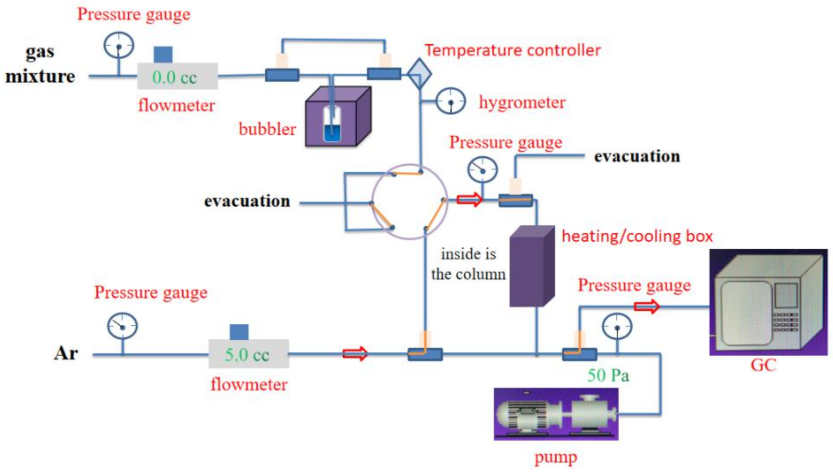

D) Under Vacuum

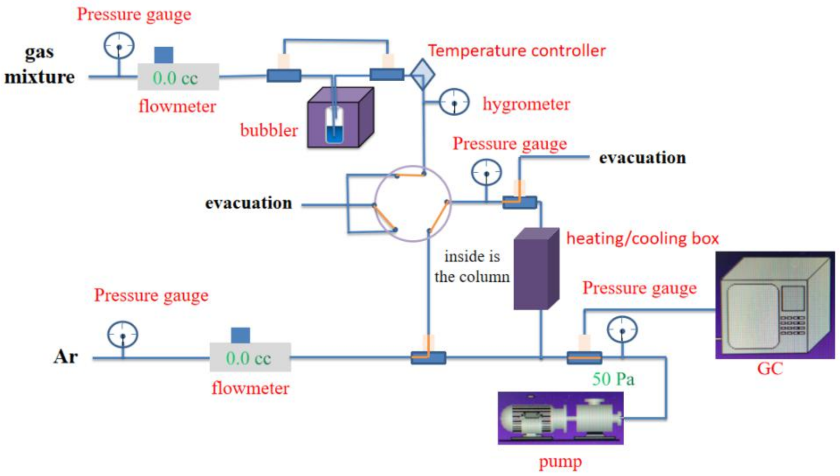

Figure S1. The illustration of the gas breakthrough equipment working mechanism containing gas pipelines, pressure gauge, flowmeter, hygrometer, GC, bubbler and pump: A) under work in dry conditions; B) under work in humid conditions; C) under purge; D) under vacuum.

Calculation of separation factor (α)

The amount of gas adsorbed i (q_i) is calculated from the breakthrough curve using the following:

$$q_i = \frac{V_T P_i \Delta T}{m}$$

Here, V_T is the total flow rate of gas (cm^3/min), P_i is the partial pressure of gas i (atm), ΔT is the time for initial breakthrough of gas i to occur (mins) and m is the mass of the sorbent (g). The separation factor (α) of the breakthrough experiment is determined as

$$\alpha = \frac{q_1 y_2}{q_2 y_1}$$

Where, y_i is the partial pressure of gas i in the gas mixture.

Grand canonical Monte Carlo (GCMC) simulations

GCMC simulations were performed in MS 2017R2 package using sorption module. The structure of ZNU-2 was firstly optimized *via* DFT geometry optimization. The Mulliken charges for atoms of ZNU-2 were derived from DFT calculation. The simulations adopted the locate task, Metropolis method in sorption module and the universal force field (UFF). The Qeq charges for atoms of ZNU-2 were selected in GCMC simulations. During the simulation, the framework was considered to be rigid during the simulation and the interaction energy between the adsorbed molecules and the framework were computed through the Coulomb and Lennard-Jones 6-12 (LJ) potentials. The cutoff radius was chosen 18.5 Å for Van der Walls interaction and the long range electrostatic interactions were handled using the Ewald summation method. The loading steps and the equilibration steps were 1×10^7, the production steps were 1×10^7. The cutoff radius was chosen 18.5 Å for Van der Walls interaction and the long range electrostatic interactions were handled using the Ewald summation method. The loading steps and the equilibration steps were 1×10^7, the production steps were 1×10^7.

Density functional theory (DFT) calculations

The DFT calculation were performed using the Gaussian package. The PBE0 functionals with the Grimme's D3(BJ) dispersion correction were applied to DFT calculations along with the 6-311+G(d,p) basis set. All structures were optimized without any symmetry constraints and the optimized minimum-energy structures were verified as stationary points on the potential energy surface by performing numerical harmonic vibrational frequency calculations. The equation for the calculation of binding energy (ΔE) is defined as: $\Delta E = E(MOF) + E(gas) - E(MOF+gas)$.

II Characterization (SCXRD, PXRD, TGA)

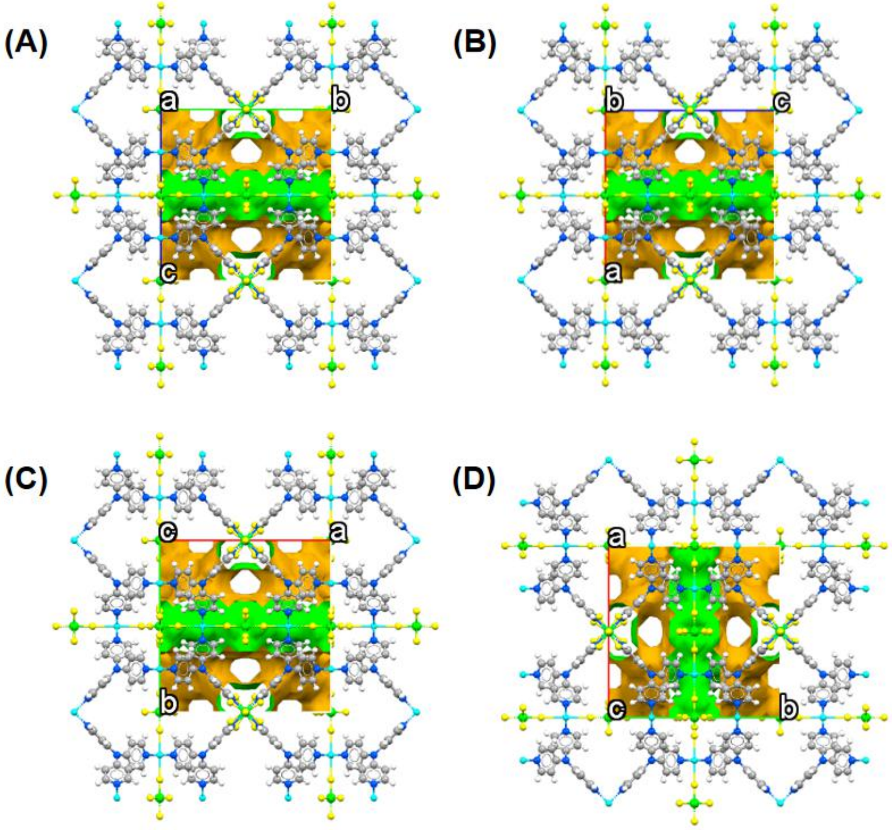

Figure S2. 1×1×1 packing diagrams of ZNU-2 viewed down the crystallographic *a*-, *b*-, *c*-axis (a, b, c) and x+90 in ball-stick mode with pore surface in green representing the inside and yellow the outside determined using a probe of 1.2 Å by PLATON.

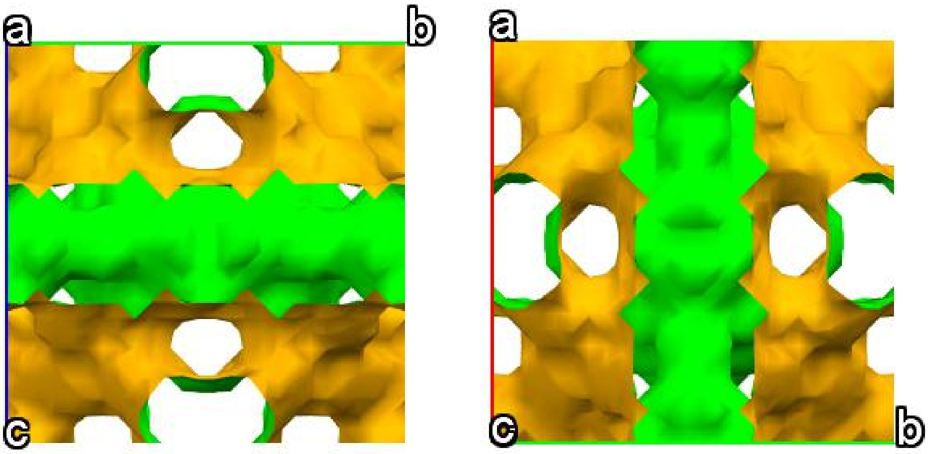

Figure S3. Void surface of ZNU-2 viewed down the crystallographic *a*-axis and x+90.

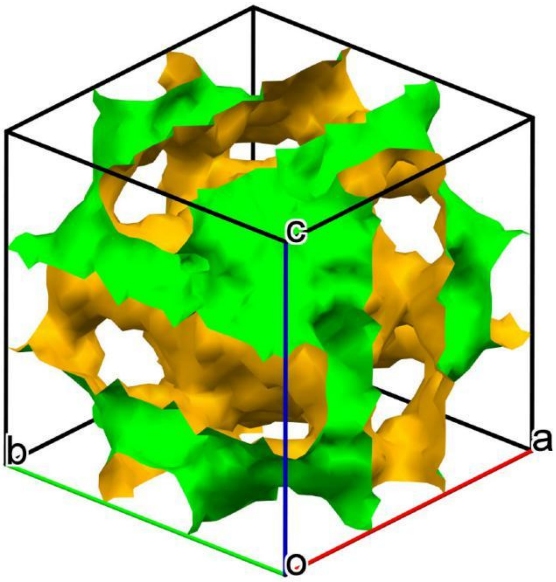

Figure S4. Void surface of ZNU-2.

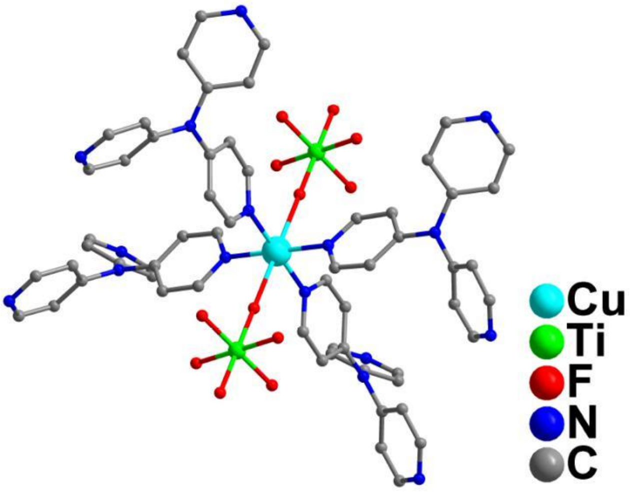

Figure S5. The Cu(II) coordination environment of ZNU-2.

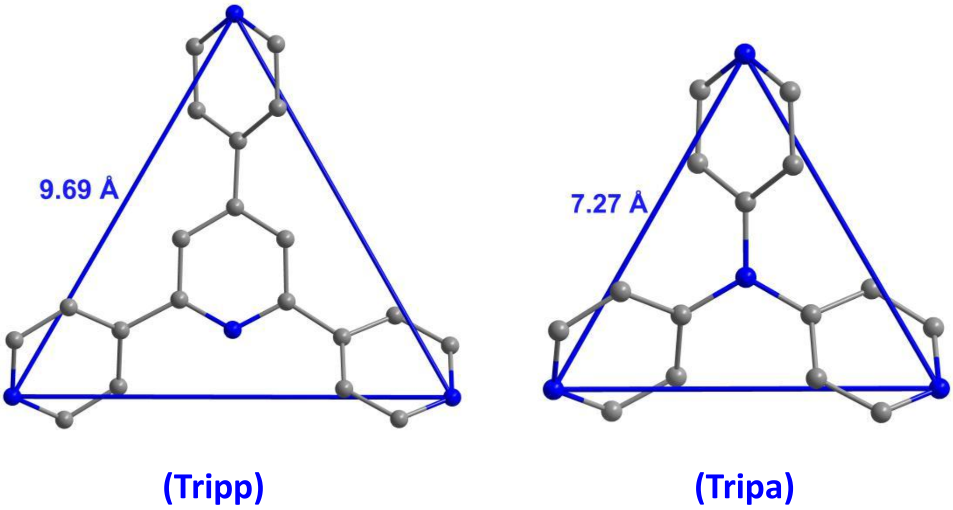

Figure S6. The size of two different tridentate ligands.

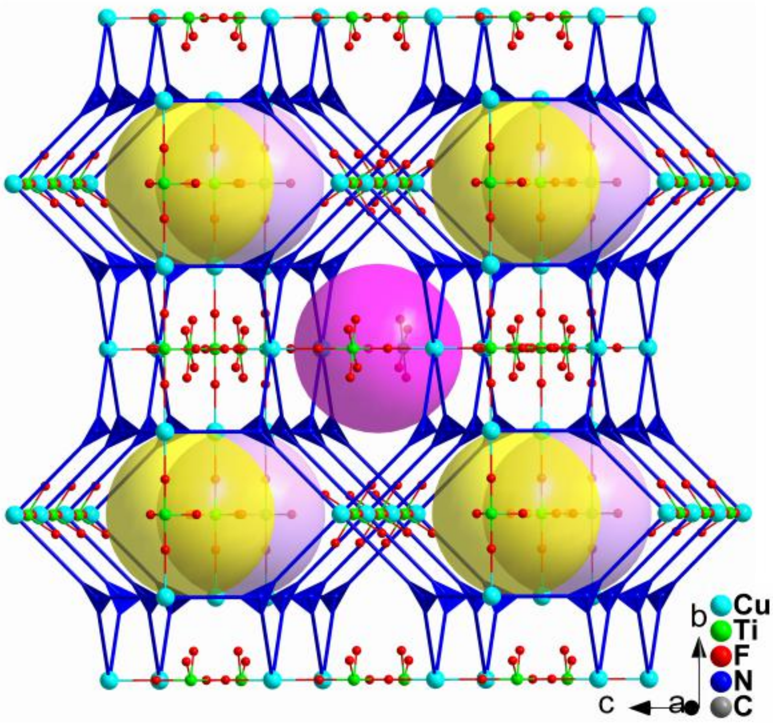

Figure S7. Structure of ZNU-2 with cage-like pores.

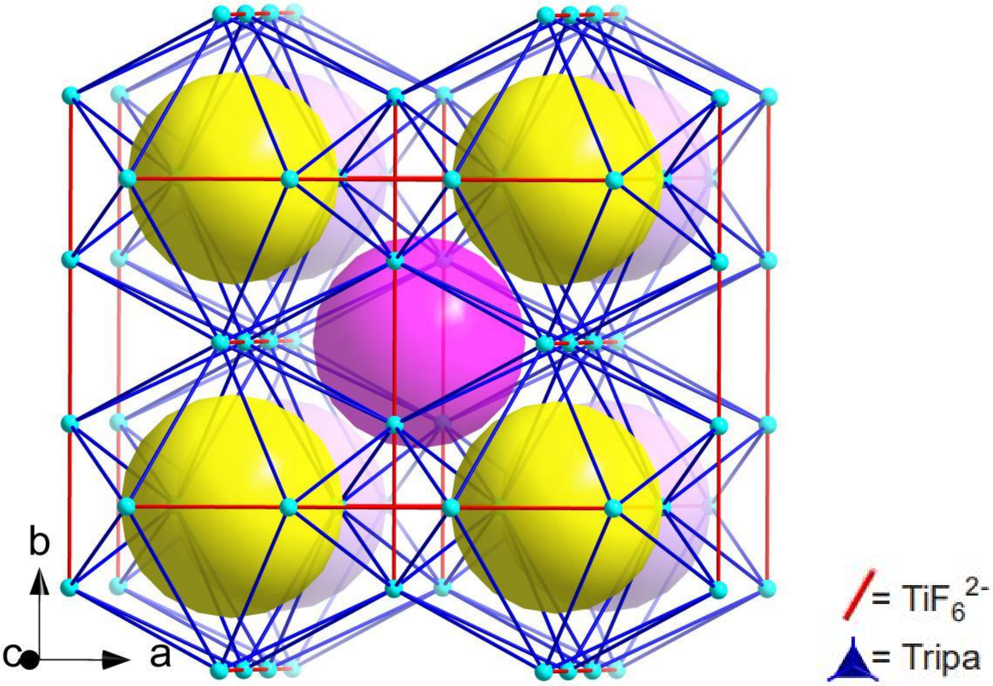

Figure S8. Structure of icosahedral Cu(II) cage.

Table S1 Crystallographic parameters of ZNU-2.

Materials	ZNU-2
Cell	a=17.5855(9)
	b=17.5855(9)
	c=17.5855(9)
	α=90
	β=90
	γ=90
Temperature	173 K
Volume (Å^3)	5438.3(8)
Space group	Pm-3n
Hall group	-P 4n 2 3
formula	$C_{20}H_{16}CuF_6N_{5.33}Ti$
MW	556.49
density	1.020
Z	6
R	0.0586(989)
wR2	0.1890(1137)
S	1.148

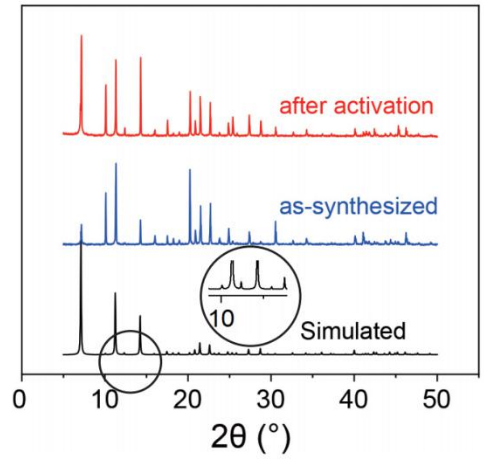

Figure S9. PXRD patterns of ZNU-2. The PXRD patterns for the simulated sample and fresh MOF match very well regardless of the peak intensity.

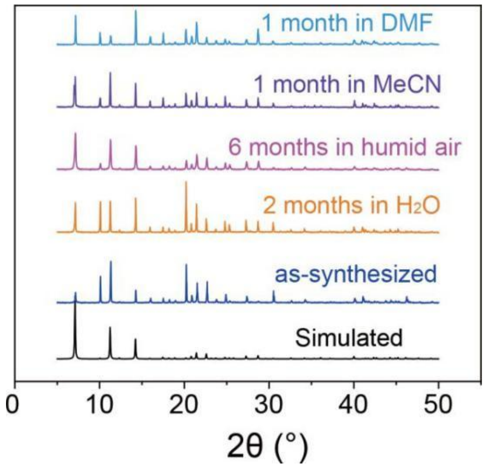

Figure S10. PXRD patterns of ZNU-2 after different treatment.

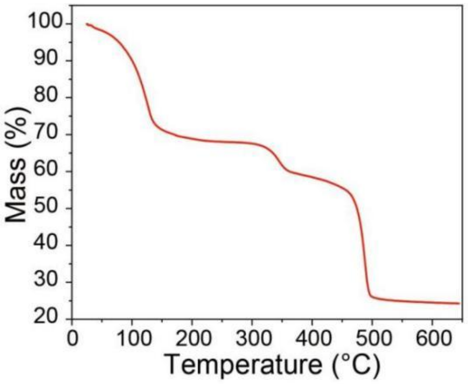

Figure S11. TGA curve of ZNU-2. The weight loss between 50-110 ºC is because of the loss of MeOH and water from the sample. The weight keeps consistent until ~308 ºC.

III Adsorption data, IAST selectivity and *Qst*

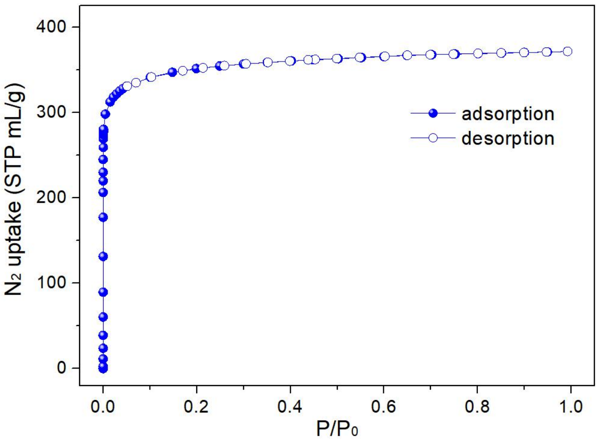

Figure S12. The adsorption and desorption isotherm of N_2 on ZNU-2 at 77 K.

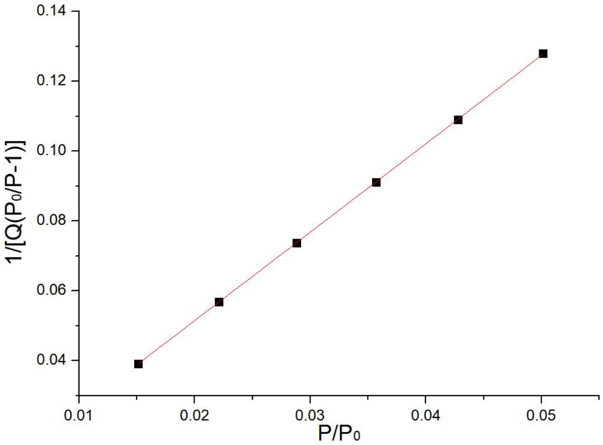

Figure S13. Plot for the calculation of the BET surface area..

The BET surface area calculated from the N_2 adsorption isotherms under the pressure range of P/P_0 = 0.01-0.05 (for micropores) is 1380 m^2/g.

MBET summary:

Slope = 2.523;

Intercept = 1.084×10^{-3};

Correlation coefficient, r= 0.999996;

C constant = 2328.003

Table S2. Comparison of C_3H_4 and C_3H_6

Gas molecules	Kinetic Diameter (Å)	Molecular size (Å^3)	Boiling point (K)	Polarizability (×10^{-25} cm^3)
C_3H_4	4.2	4.16 x 4.01 x 6.51	249.95	55.5
C_3H_6	4.6	4.65 x 4.16 x 6.44	225.45	62.6

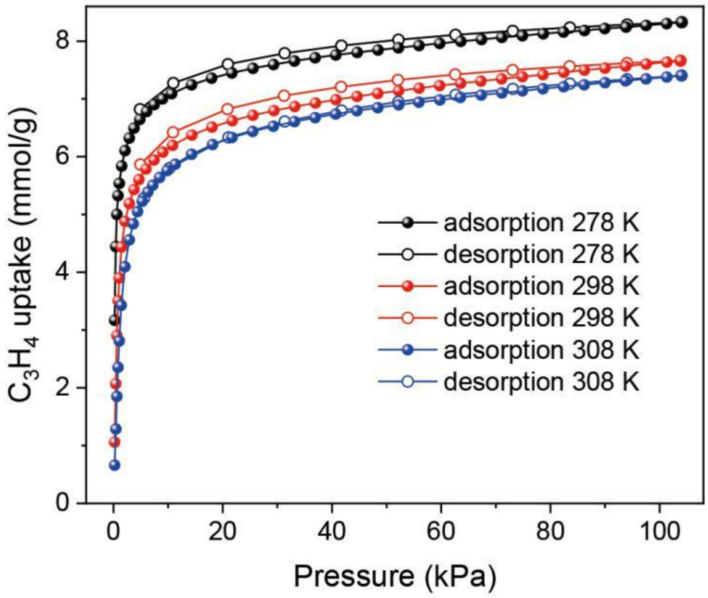

Figure S14. The sorption isotherm of C_3H_4 on ZNU-2 at 278, 298, and 308 K.

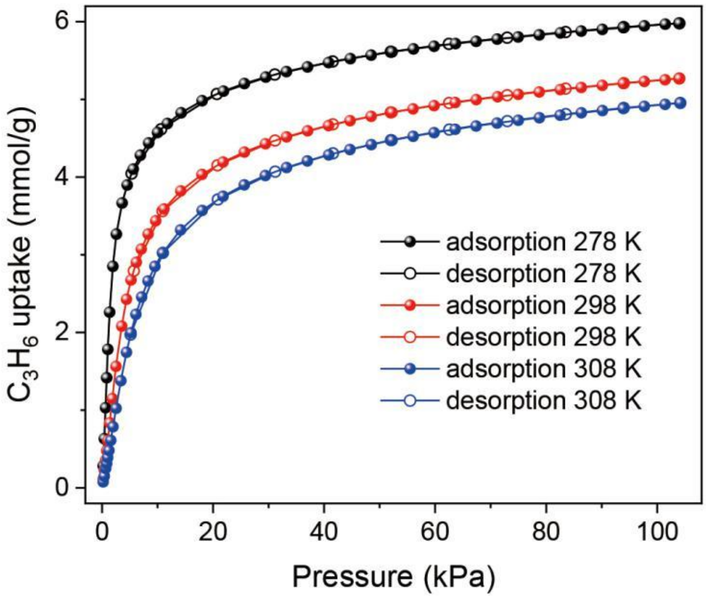

Figure S15. The sorption isotherm of C_3H_6 on ZNU-2 at 278, 298, and 308 K

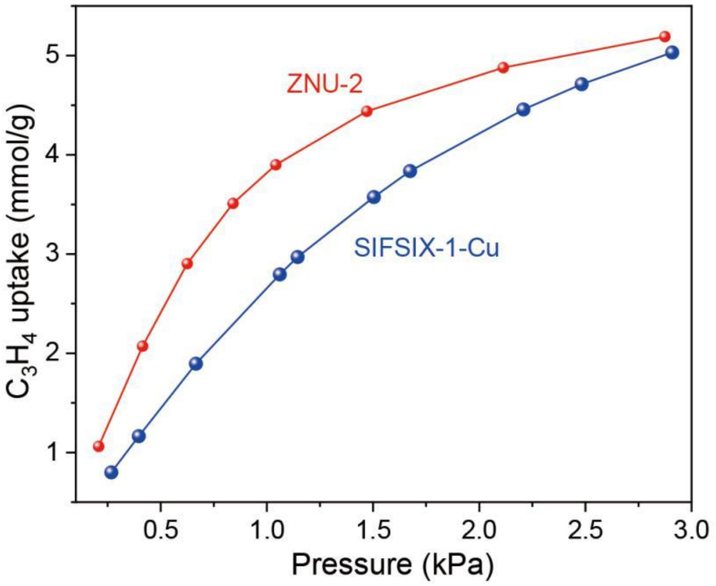

Figure S16. The adsorption isotherm of C_3H_4 on ZNU-2 and SIFSIX-1-Cu at 298 K, 0-3.0 kPa.

Table S3. Dual-site Langmuir-Freundlich fits (temperature-dependent) for C_3H_4, and C_3H_6 in ZNU-2.

	Site A				Site B			
	$q_{A,sat}$ mol/kg	b_{A0} Pa^{-1}	E_A kJ/mol	νA	$q_{B,sat}$ mol/kg	b_{B0} Pa^{-1}	E_B kJ/mol	νB
C_3H_4	6	1.387E-13	53.3	1.24	2.5	3.443E-13	44.2	1
C_3H_6	4.4	3.417E-13	44.4	1.3	2.1	6.722E-14	46	1

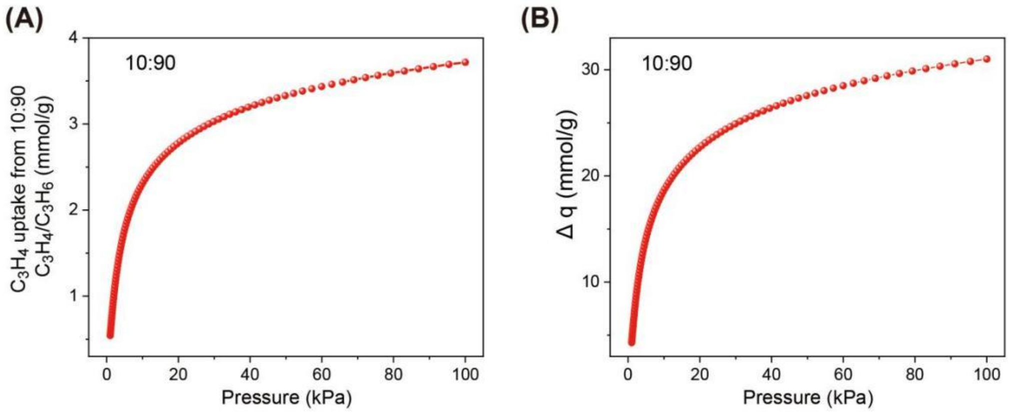

Figure S17. (A) The adsorption isotherm of C_3H_4 from C_3H_4/C_3H_6 (10/90) mixture on ZNU-2. (B) IAST based separation potential for C_3H_4/C_3H_6 (10/90) mixtures.

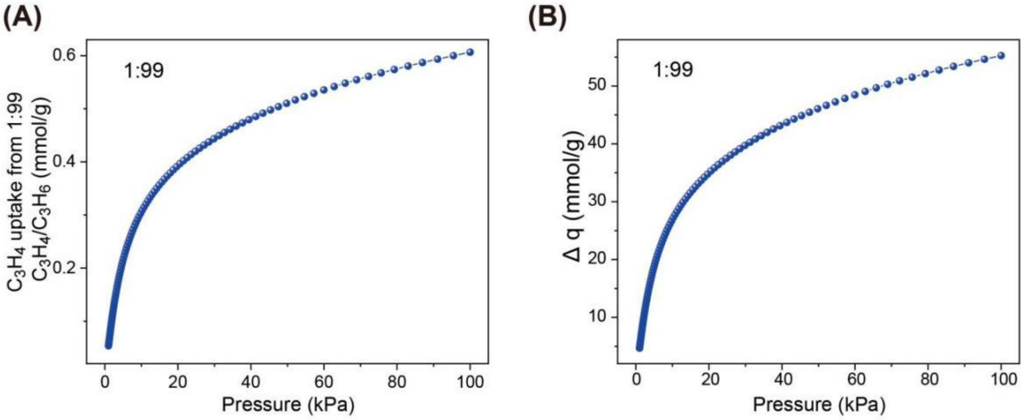

Figure S18. (A) The adsorption isotherm of C_3H_4 from C_3H_4/C_3H_6 (1/99) mixture on ZNU-2. (B) IAST based separation potential for C_3H_4/C_3H_6 (1/99) mixtures.

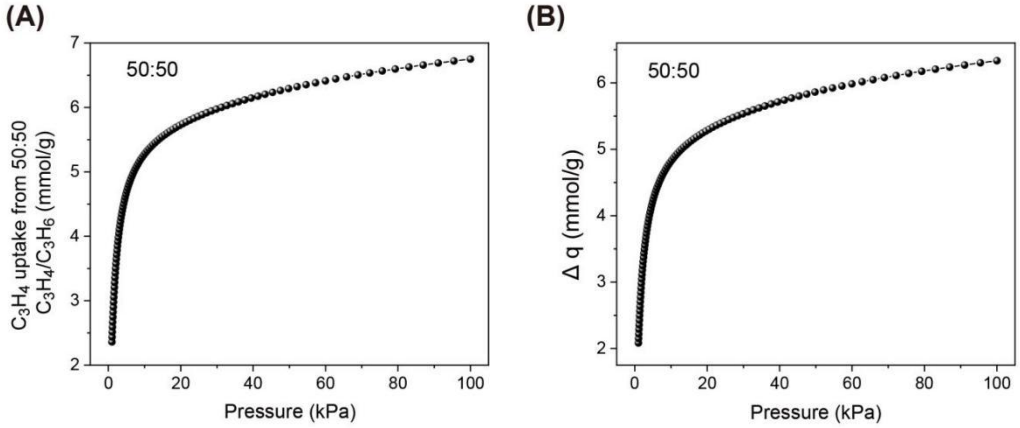

Figure S19. (A) The adsorption isotherm of C_3H_4 from C_3H_4/C_3H_6 (50/50) mixture on ZNU-2. (B) IAST based separation potential for C_3H_4/C_3H_6 (50/50) mixtures.

Table S4. Dual-site Langmuir-Freundlich fits (temperature-independent) for C_3H_4, and C_3H_6 in ZNU-2.

	Site A			Site B			Correlation Coefficient (R^2)
	$q_{A,sat}$ cc/g	b_A Pa $^{-v_A}$	$v\ A$	$q_{B,sat}$ cc/g	b_B Pa $^{-v_B}$	$v\ B$	
C_3H_4	105.5034	2.127	1.52	124.7224	0.121	0.48	0.99990739
C_3H_6	59.5568	0.1234	1.78	82.9982	0.084	0.72	0.99999739

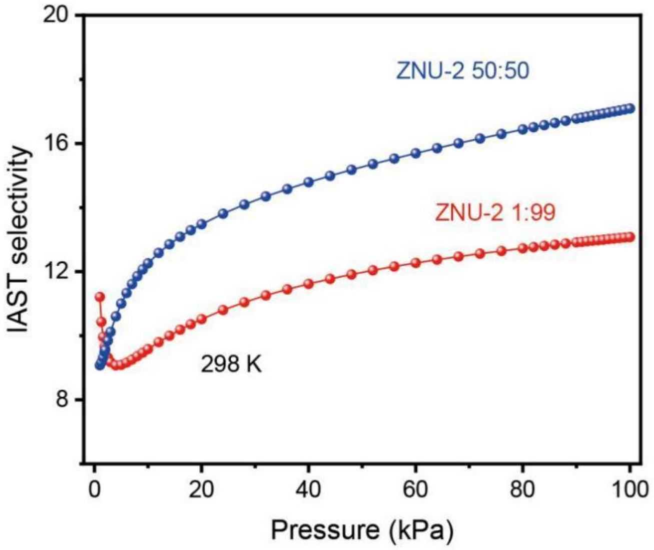

Figure S20. IAST selectivity of ZNU-2 towards gas mixtures of C_3H_4/C_3H_6 (50/50 and 1/99) at 298 K.

The IAST selectivity calculated based on the temperature-independent Dual-site Langmuir-Freundlich fits only using the 298 K isotherms was very slightly higher than that based on temperature-independent Dual-site Langmuir-Freundlich fits (in the maintext) but almost incidental.

Table S5. Unary isotherm fit parameters for C_3H_4, and C_3H_6 in SIFSIX-14-Cu-i at 298 K.

	Site A			Site B		
	$q_{A,sat}$ mol kg^{-1}	b_A $Pa^{-\nu A}$	ν_A dimensionless	$q_{B,sat}$ mol kg^{-1}	b_B $Pa^{-\nu B}$	ν_B dimensionless
C_3H_4	1.7	1.879E-03	0.64	2.2	3.746E-18	6.35
C_3H_6	1.15	2.672E-81	18	20	9.099E-06	0.67

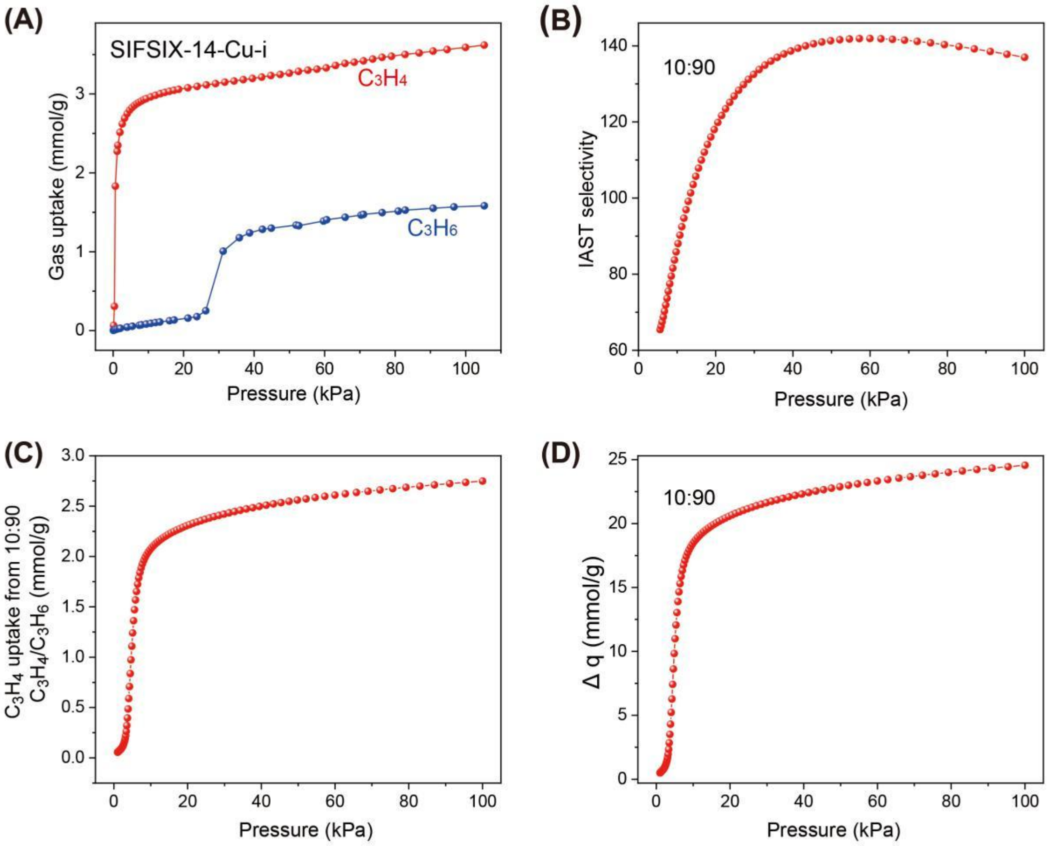

Figure S21. (A) C_3H_4 and C_3H_6 adsorption isotherms for SIFSIX-14-Cu-i at 298 K. (B) IAST selectivity of SIFSIX-14-Cu-i towards gas mixtures of C_3H_4/C_3H_6 (10/90). (C) The adsorption isotherm of C_3H_4 from C_3H_4/C_3H_6 (10/90) mixture on SIFSIX-14-Cu-i. (D) IAST based separation potential for C_3H_4/C_3H_6 (10/90) mixtures.

Table S6. Unary isotherm fit parameters for C_3H_4, and C_3H_6 in GeFSIX-14-Cu-i at 298 K.

	Site A			Site B		
	$q_{A,sat}$ mol kg^{-1}	b_A $Pa^{-\nu A}$	ν_A dimensionless	$q_{B,sat}$ mol kg^{-1}	b_B $Pa^{-\nu B}$	ν_B dimensionless
C_3H_4	1.4	3.778E-04	1	1.9	1.316E-10	4.08
C_3H_6	1.12	1.183E-45	10	4	5.019E-05	0.65

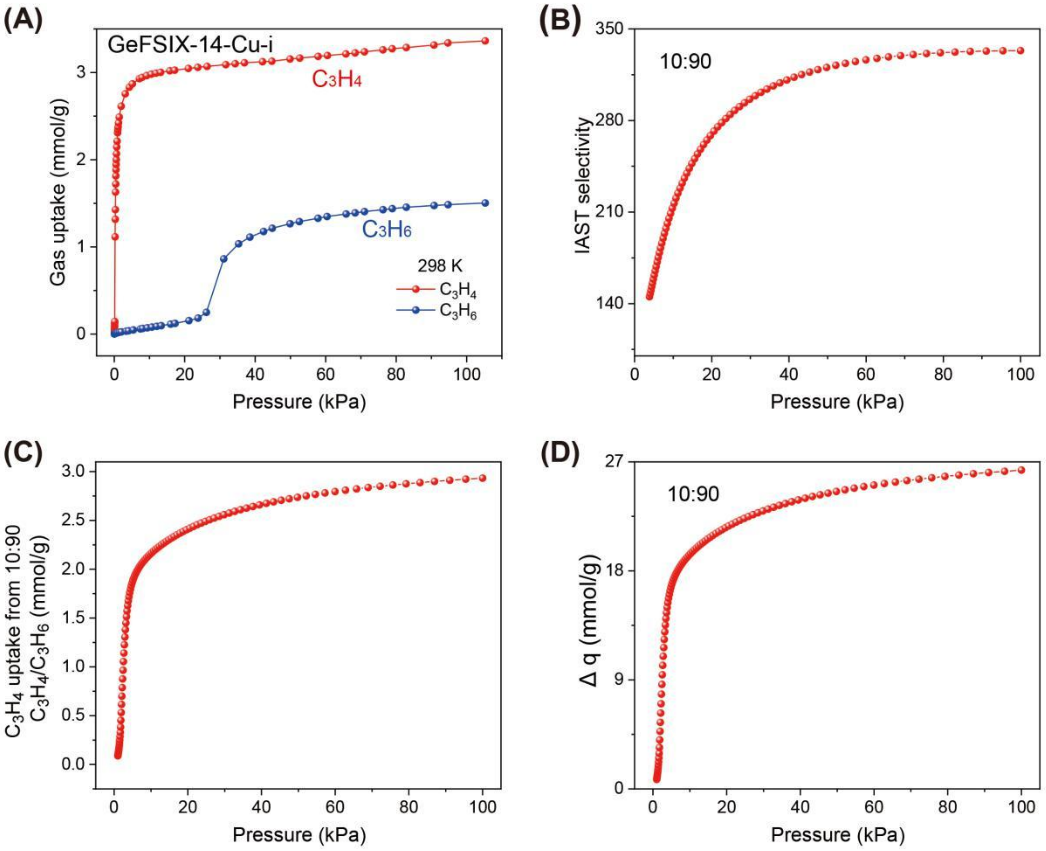

Figure S22. (A) C_3H_4 and C_3H_6 adsorption isotherms for GeFSIX-14-Cu-i at 298 K. (B) IAST selectivity of GeFSIX-14-Cu-i towards gas mixtures of C_3H_4/C_3H_6 (10/90). (C) The adsorption isotherm of C_3H_4 from C_3H_4/C_3H_6 (10/90) mixture on GeFSIX-14-Cu-i. (D) IAST based separation potential for C_3H_4/C_3H_6 (10/90) mixtures.

Table S7. Unary isotherm fit parameters for C_3H_4, and C_3H_6 in TIFSIX-14-Cu-i at 298 K.

	Site A			Site B		
	$q_{A,sat}$ mol kg^{-1}	b_A Pa$^{-\nu A}$	ν_A dimensionless	$q_{B,sat}$ mol kg^{-1}	b_B Pa$^{-\nu B}$	ν_B dimensionless
C_3H_4	2	3.869E-04	1	1.5	8.723E-07	3
C_3H_6	1.77	4.129E-06	1.2			

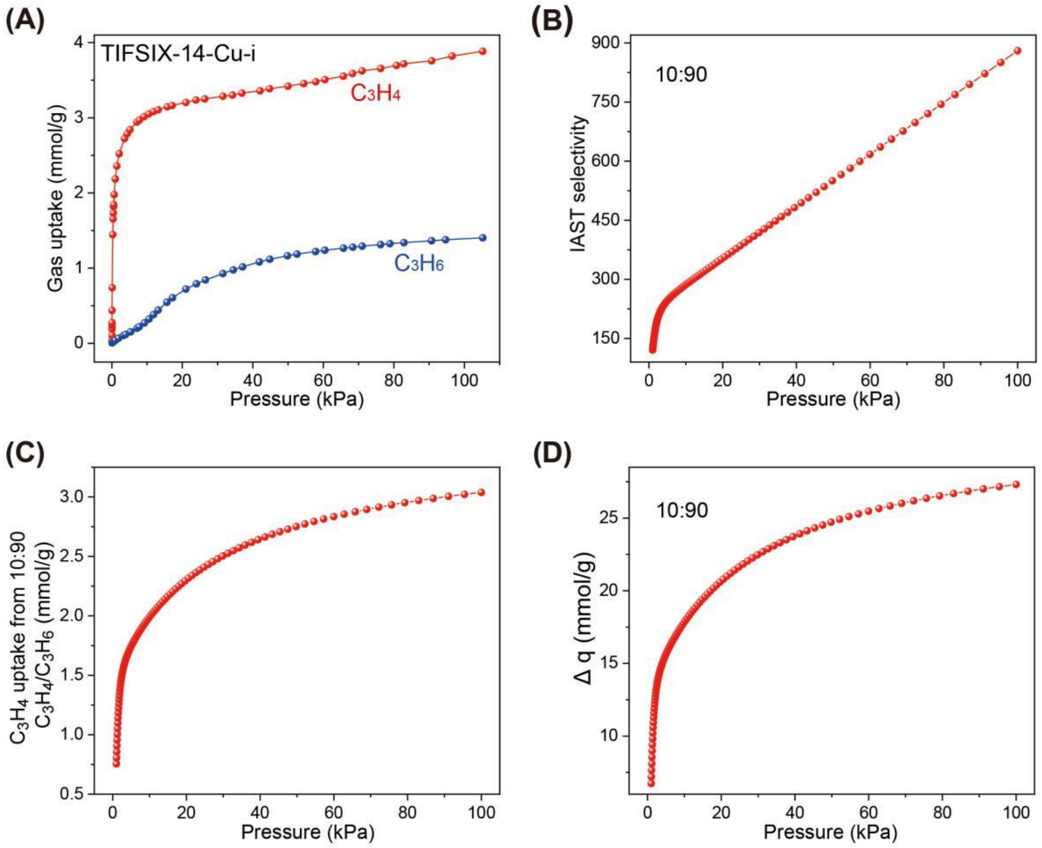

Figure S23. (A) C_3H_4 and C_3H_6 adsorption isotherms for TIFSIX-14-Cu-i at 298 K. (B) IAST selectivity of TIFSIX-14-Cu-i towards gas mixtures of C_3H_4/C_3H_6 (10/90). (C) The adsorption isotherm of C_3H_4 from C_3H_4/C_3H_6 (10/90) mixture on TIFSIX-14-Cu-i. (D) IAST based separation potential for C_3H_4/C_3H_6 (10/90) mixtures.

Table S8. Unary isotherm fit parameters for C_3H_4 and C_3H_6 in SIFSIX-1-Cu at 298 K.

	Site A			Site B		
	$q_{A,sat}$ mol kg^{-1}	b_A $Pa^{-\nu A}$	ν_A dimensionless	$q_{B,sat}$ mol kg^{-1}	b_B $Pa^{-\nu B}$	ν_B dimensionless
C_3H_4	8	5.815E-07	1	8.4	4.451E-04	1
C_3H_6	2.4	7.168E-10	2.45	4	6.642E-05	1

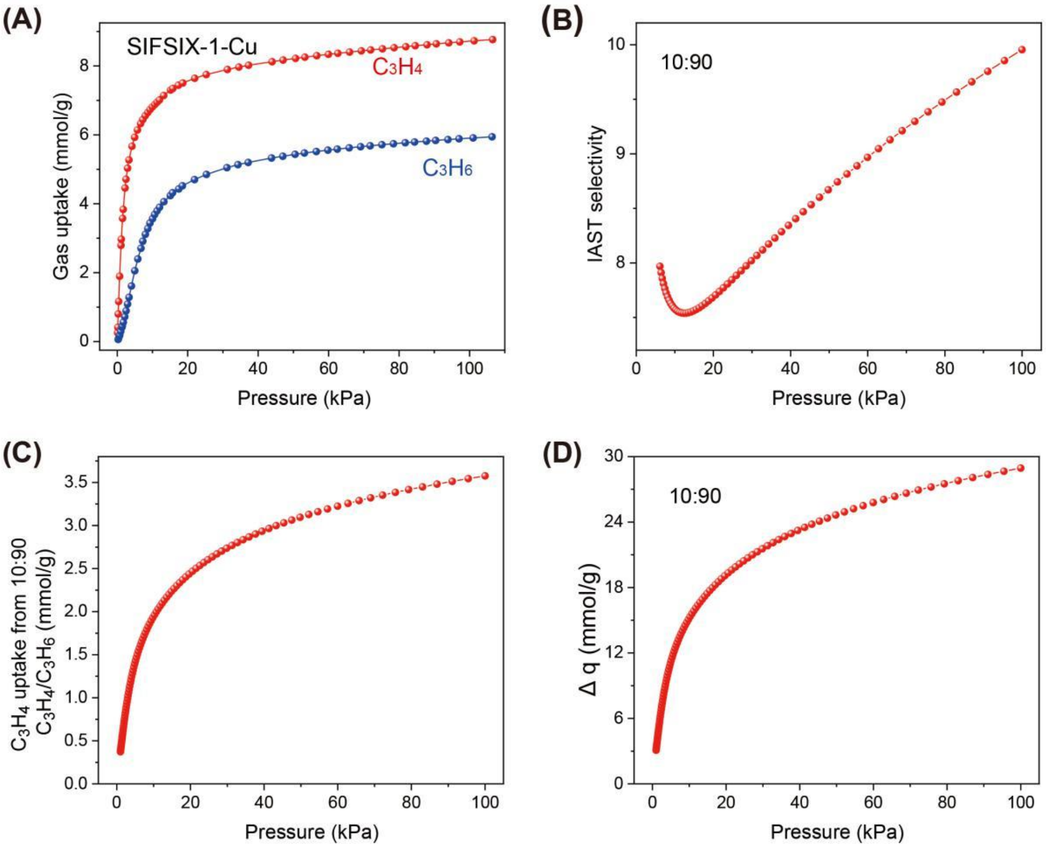

Figure S24. (A) C_3H_4 and C_3H_6 adsorption isotherms for SIFSIX-1-Cu at 298 K. (B) IAST selectivity of SIFSIX-1-Cu towards gas mixtures of C_3H_4/C_3H_6 (10/90). (C) The adsorption isotherm of C_3H_4 from C_3H_4/C_3H_6 (10/90) mixture on SIFSIX-1-Cu. (D) IAST based separation potential for C_3H_4/C_3H_6 (10/90) mixtures.

Table S9. Unary isotherm fit parameters for C_3H_4 and C_3H_6 in SIFSIX-2-Cu-i at 298 K.

	Site A			Site B		
	$q_{A,sat}$ mol kg^{-1}	b_A $Pa^{-\nu A}$	ν_A dimensionless	$q_{B,sat}$ mol kg^{-1}	b_B $Pa^{-\nu B}$	ν_B dimensionless
C_3H_4	8.2	1.544E-06	1	3.5	1.390E-03	1
C_3H_6	1.1	1.248E-04	1	2.3	3.052E-05	1

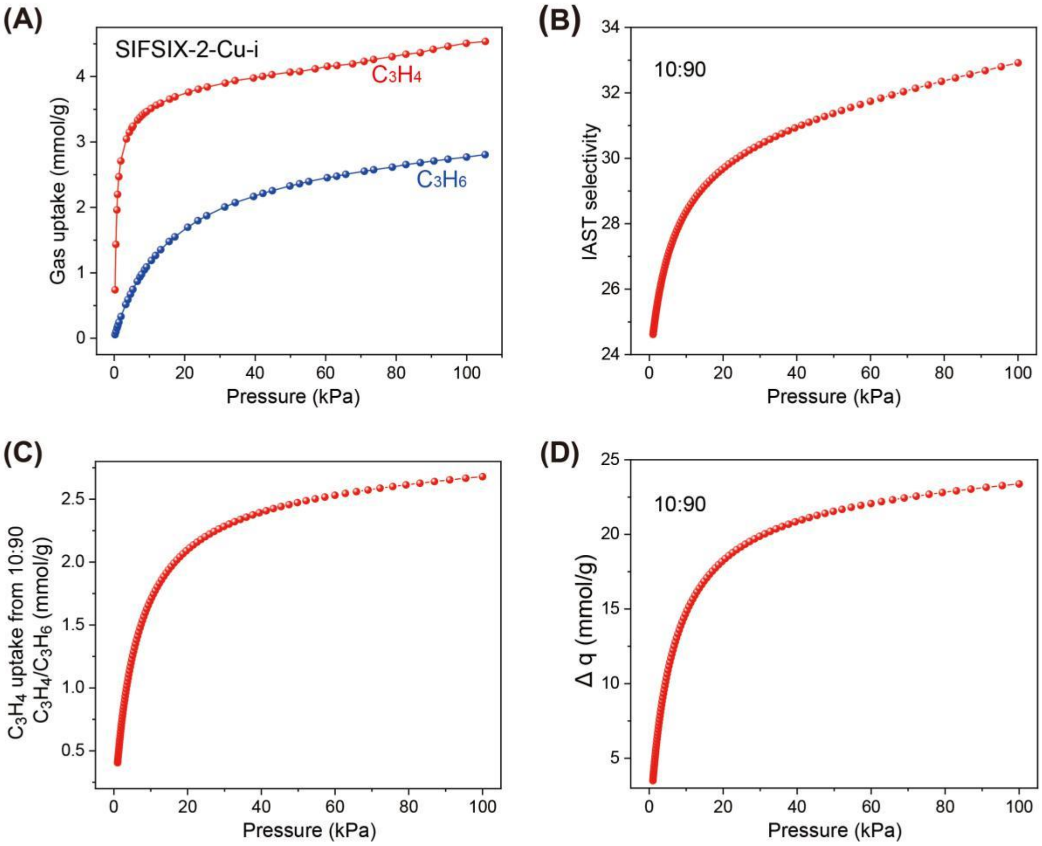

Figure S25. (A) C_3H_4 and C_3H_6 adsorption isotherms for SIFSIX-2-Cu-i at 298 K. (B) IAST selectivity of SIFSIX-2-Cu-i towards gas mixtures of C_3H_4/C_3H_6 (10/90). (C) The adsorption isotherm of C_3H_4 from C_3H_4/C_3H_6 (10/90) mixture on SIFSIX-2-Cu-i. (D) IAST based separation potential for C_3H_4/C_3H_6 (10/90) mixtures.

Table S10. Unary isotherm fit parameters for C_3H_4 and C_3H_6 in SIFSIX-3-Ni at 298 K.

	Site A			Site B		
	$q_{A,sat}$ mol kg^{-1}	b_A Pa$^{-\nu A}$	ν_A dimensionless	$q_{B,sat}$ mol kg^{-1}	b_B Pa$^{-\nu B}$	ν_B dimensionless
C_3H_4	0.6	6.453E-03	0.42	2.65	7.240E-04	2
C_3H_6	2.8	1.152E-05	1.23			

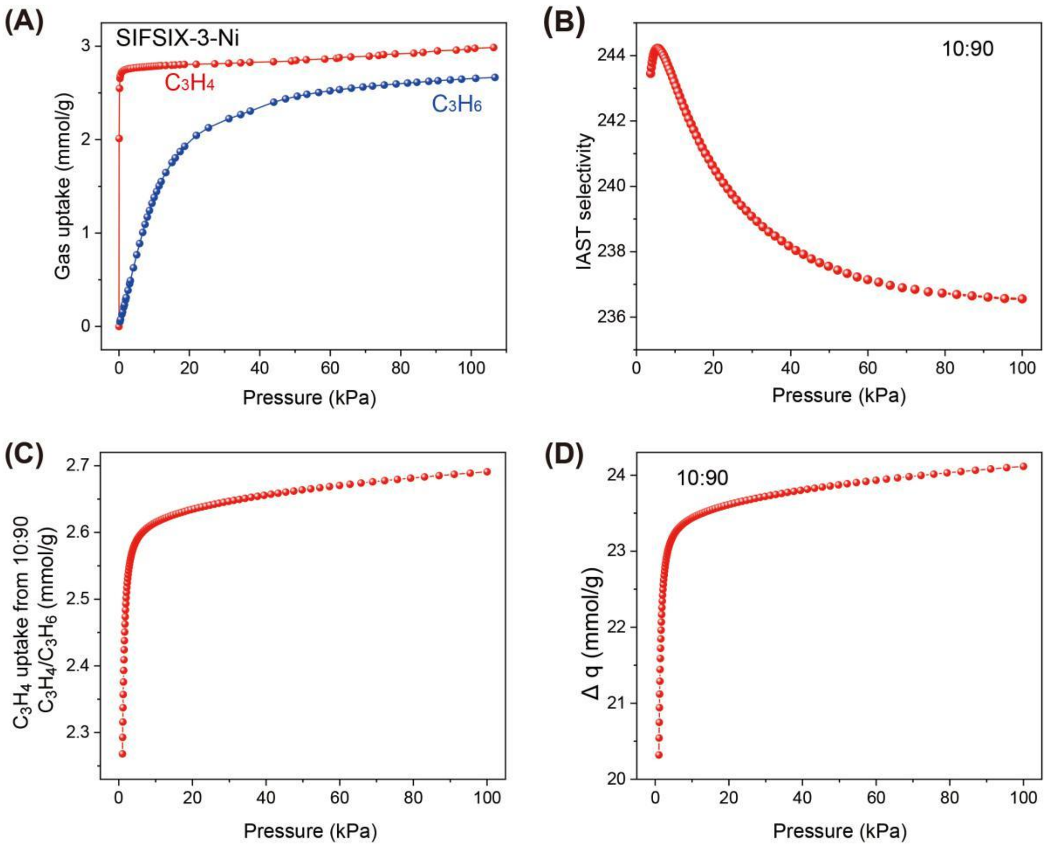

Figure S26. (A) C_3H_4 and C_3H_6 adsorption isotherms for SIFSIX-3-Ni at 298 K. (B) IAST selectivity of SIFSIX-3-Ni towards gas mixtures of C_3H_4/C_3H_6 (10/90). (C) The adsorption isotherm of C_3H_4 from C_3H_4/C_3H_6 (10/90) mixture on SIFSIX-3-Ni. (D) IAST based separation potential for C_3H_4/C_3H_6 (10/90) mixtures.

Table S11. Unary isotherm fit parameters for C_3H_4, and C_3H_6 in ZU-62 at 298 K.

	Site A			Site B		
	$q_{A,sat}$ mol kg^{-1}	b_A Pa$^{-\nu A}$	ν_A dimensionless	$q_{B,sat}$ mol kg^{-1}	b_B Pa$^{-\nu B}$	ν_B dimensionless
C_3H_4	8	4.965E-04	0.47	2.8	3.564E-03	1
C_3H_6	0.8	3.313E-17	4.6	2.3	4.092E-05	1

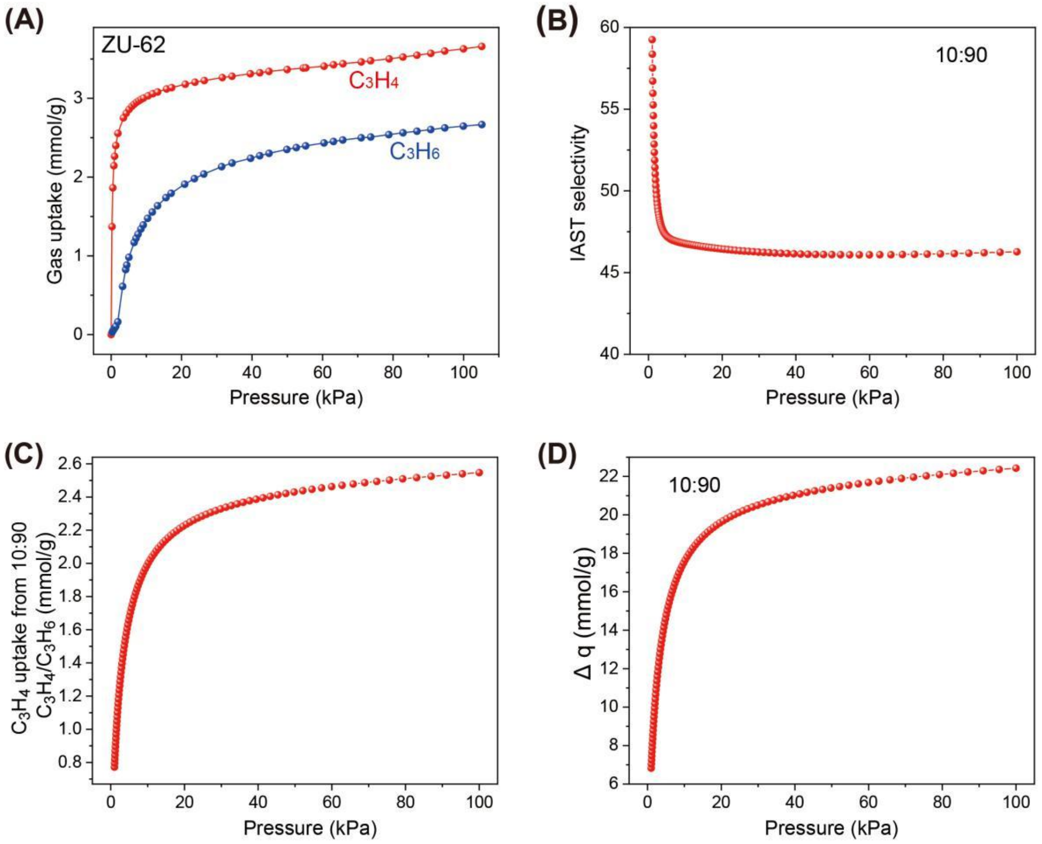

Figure S27. (A) C_3H_4 and C_3H_6 adsorption isotherms for ZU-62 at 298 K. (B) IAST selectivity of ZU-62 towards gas mixtures of C_3H_4/C_3H_6 (10/90). (C) The adsorption isotherm of C_3H_4 from C_3H_4/C_3H_6 (10/90) mixture on ZU-62. (D) IAST based separation potential for C_3H_4/C_3H_6 (10/90) mixtures.

IV DFT Calculation & GCMC simulation

Table S12. Labels of the figures of DFT calculation and GCMC simulation

● C ○ H ● F ● N ● Cu ● Ti ● $C(C_3H_4)$ ⬡ Py(cage 1) ⬡ Py(cage 2)	⋰ $F\cdots H(C_3H_4)$ ⋰ $C(C_3H_4)\cdots H(Py)$ ⋰ $H(C_3H_4)\cdots H(Py)$ ⋰ $C(C_3H_4)\cdots C(Py)$ ⋰ $H(C_3H_4)\cdots C(C_3H_4)$ ⋰ $H(C_3H_4)\cdots C(Py)$

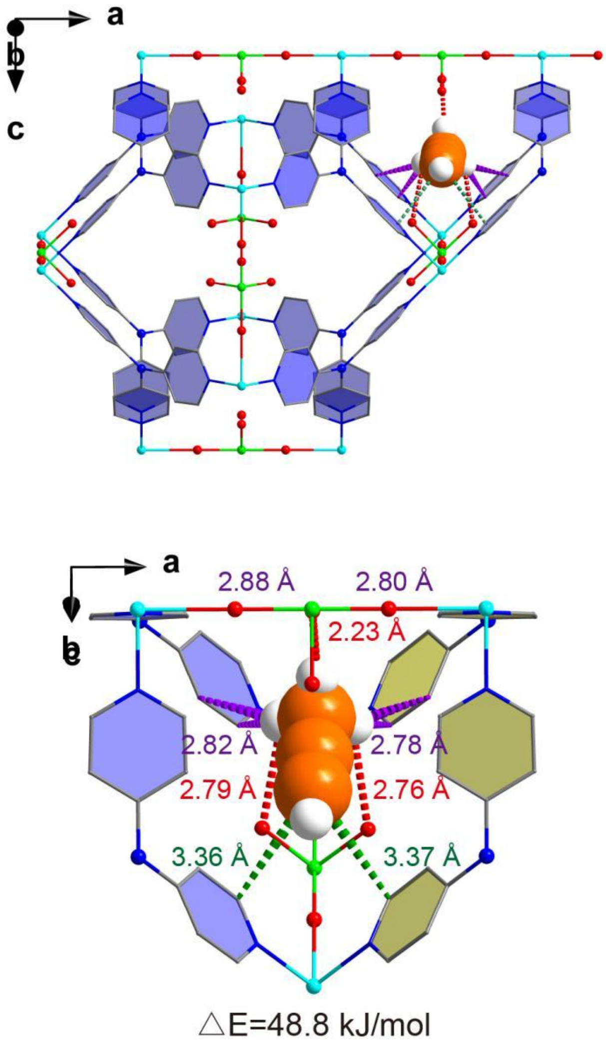

Figure S28. The DFT-D optimized adsorption configuration of C_3H_4 in the first binding site perpendicular to the channel between two cages.

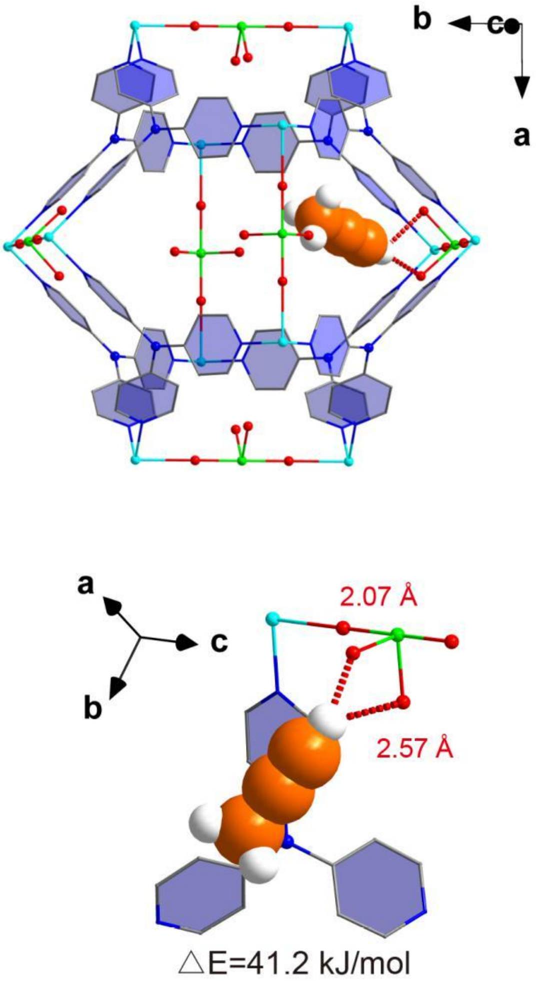

Figure S29. The DFT-D optimized adsorption configuration of C_3H_4 in the second binding site in the cage.

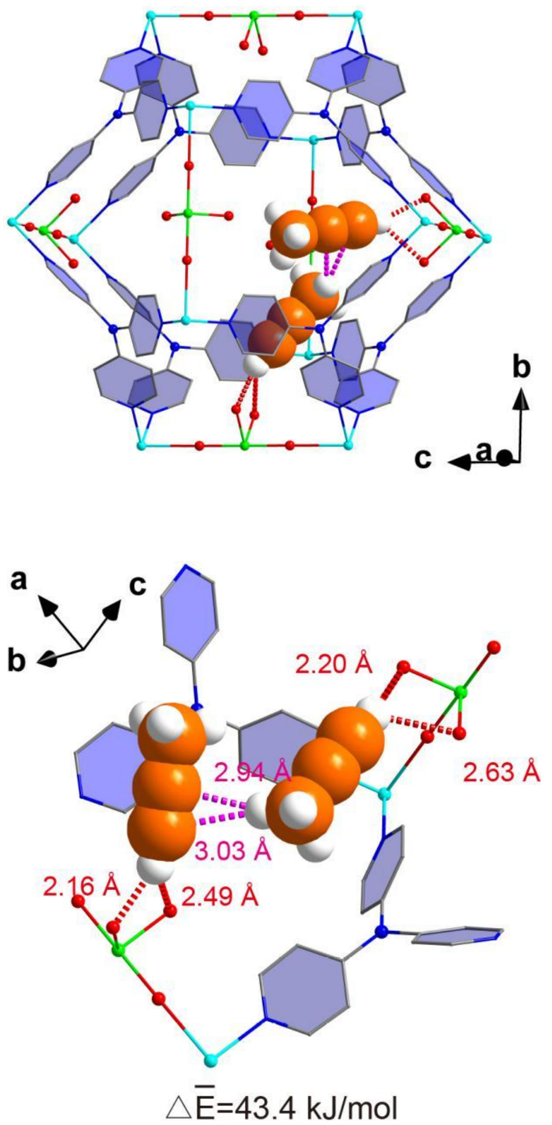

Figure S30. The DFT-D optimized adsorption configuration of two C_3H_4 molecules in the cage.

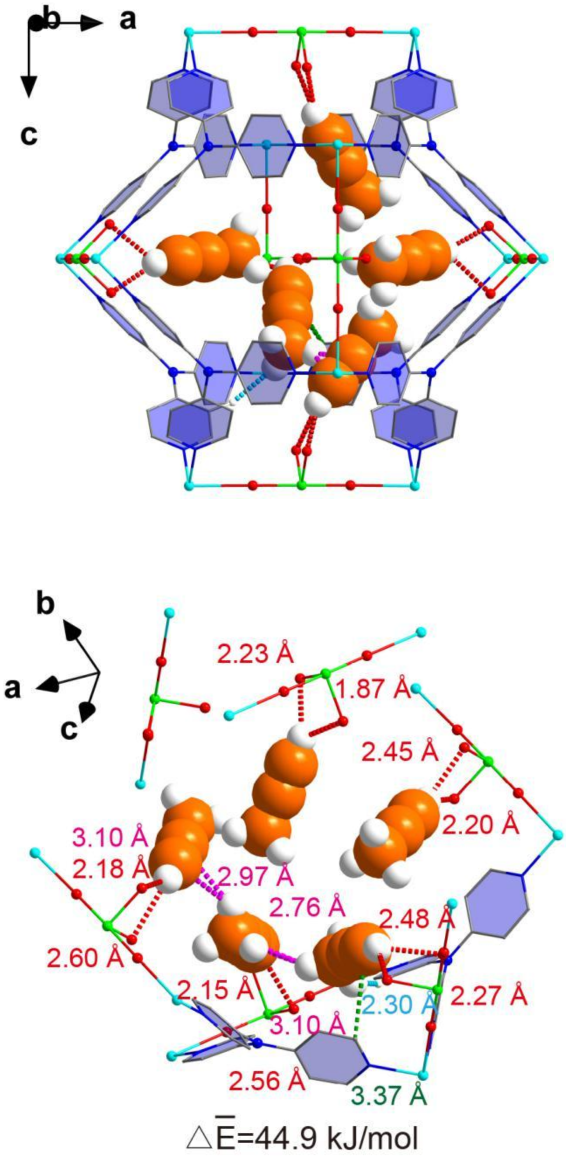

Figure S31. The DFT-D optimized adsorption configuration of five C_3H_4 molecules in the cage.

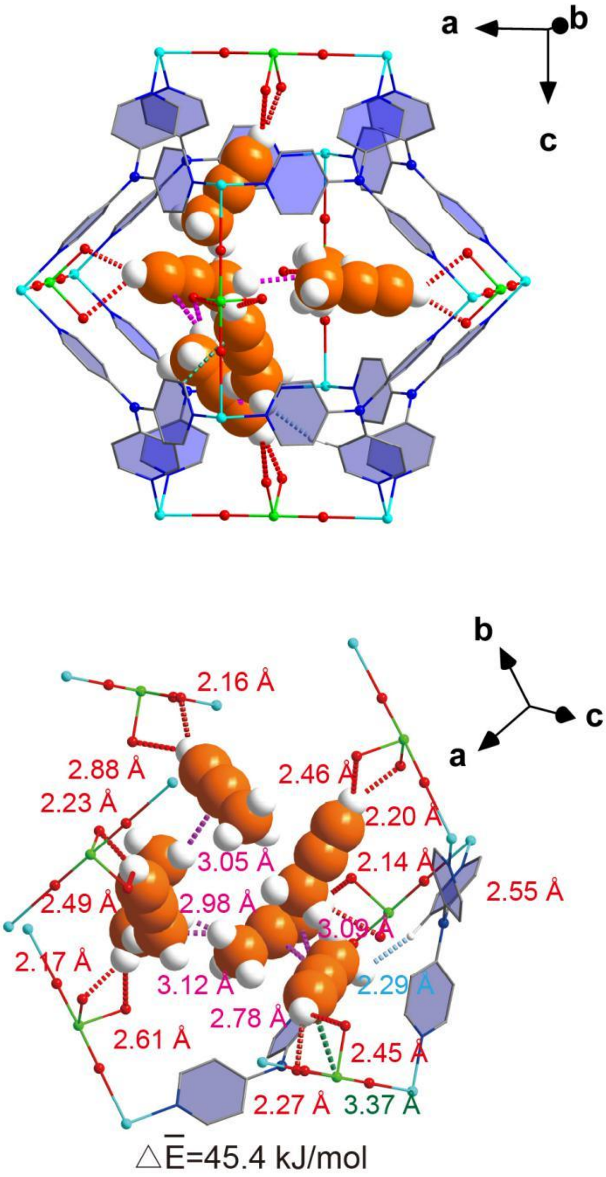

Figure S32. The DFT-D optimized adsorption configuration of six C_3H_4 molecules in the cage.

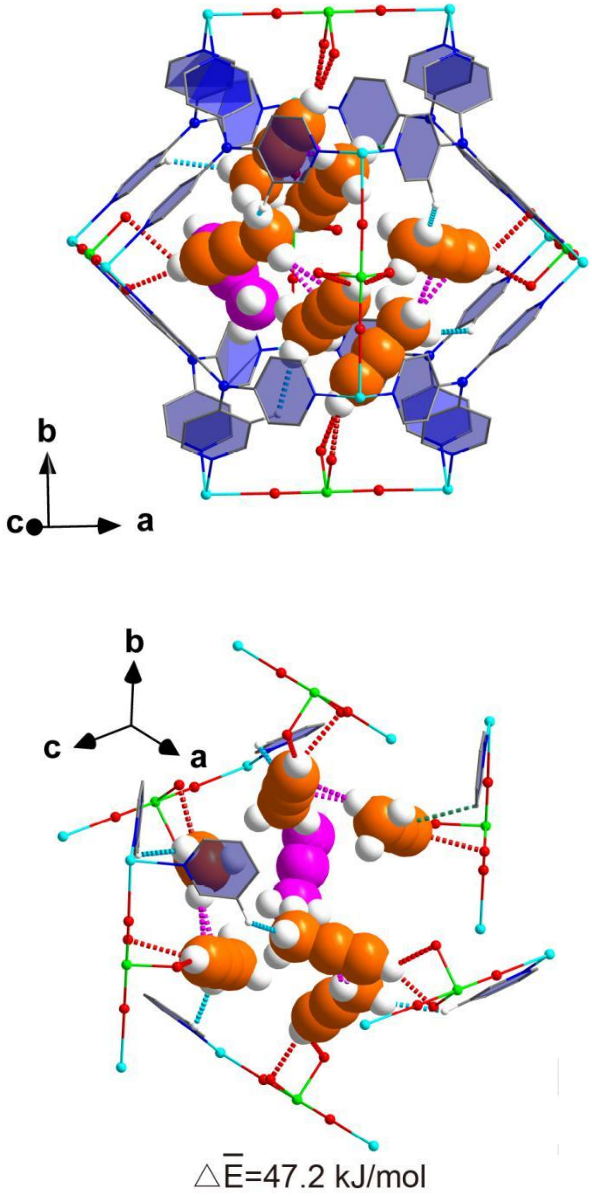

Figure S33. The DFT-D optimized adsorption configuration of seven C_3H_4 molecules in the cage.

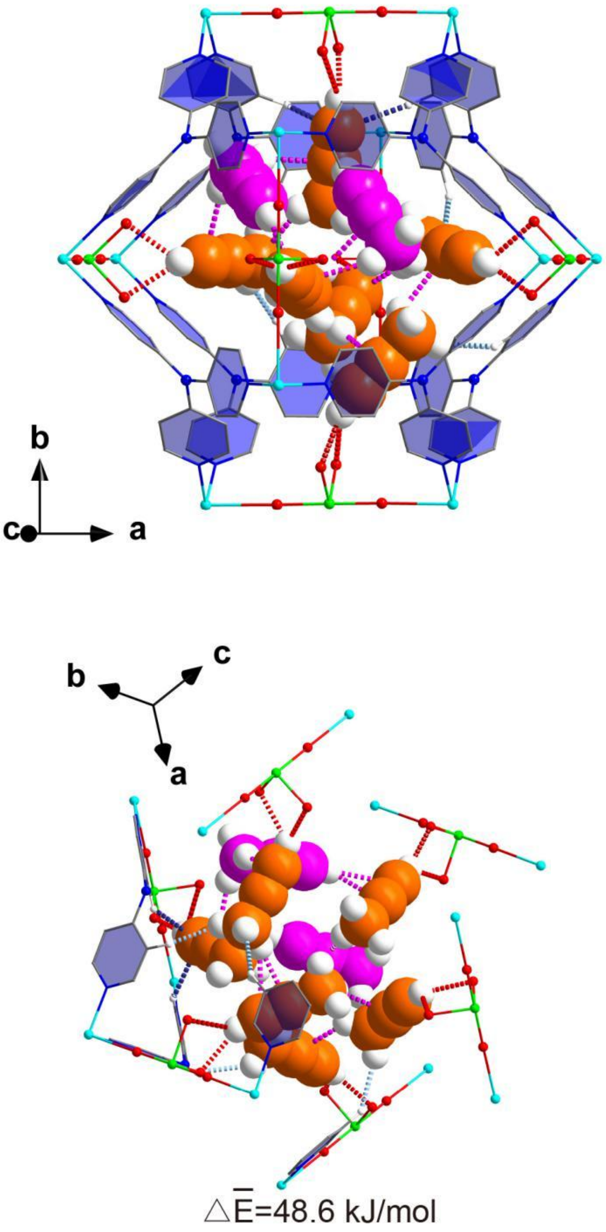

Figure S34. The DFT-D optimized adsorption configuration of eight C_3H_4 molecules in the cage.

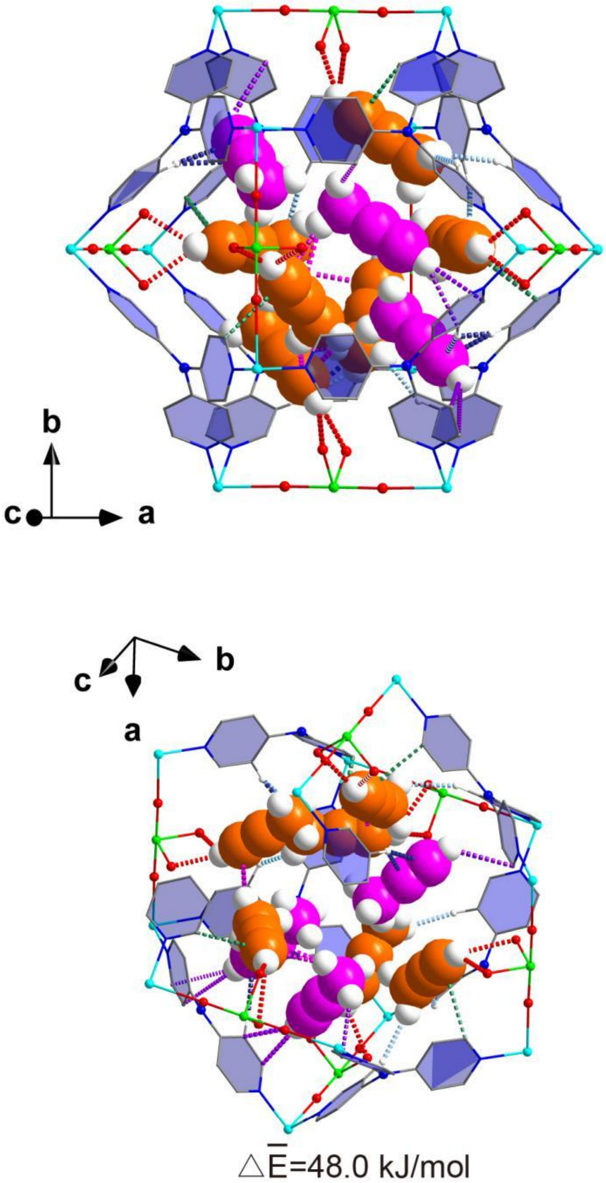

Figure S35. The DFT-D optimized adsorption configuration of nine C_3H_4 molecules in the cage.

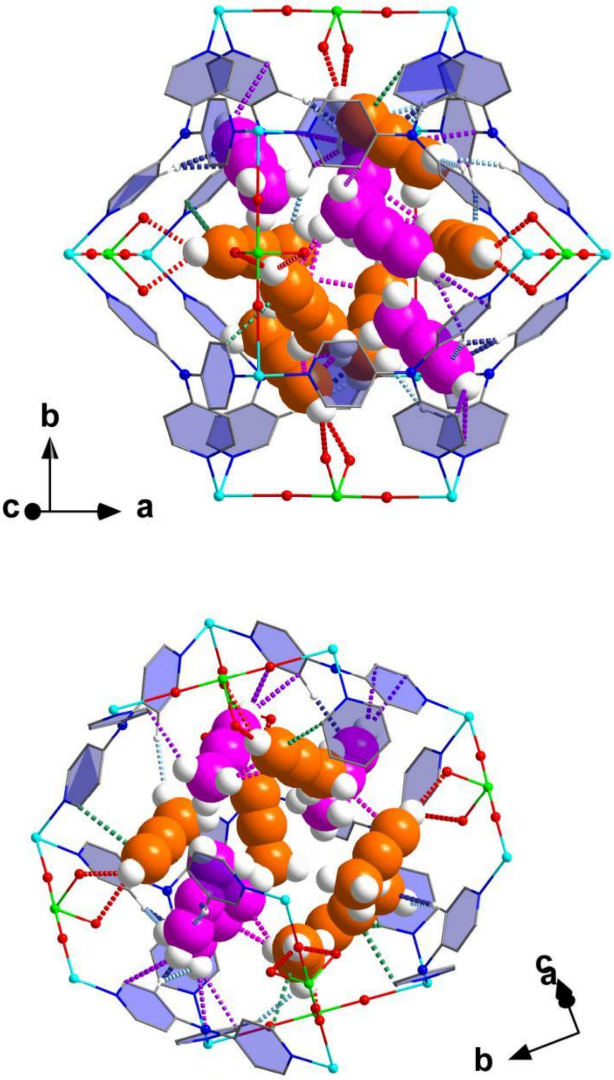

$\triangle\overline{E}$=47.0 kJ/mol

Figure S36. The DFT-D optimized adsorption configuration of ten C_3H_4 molecules in the cage.

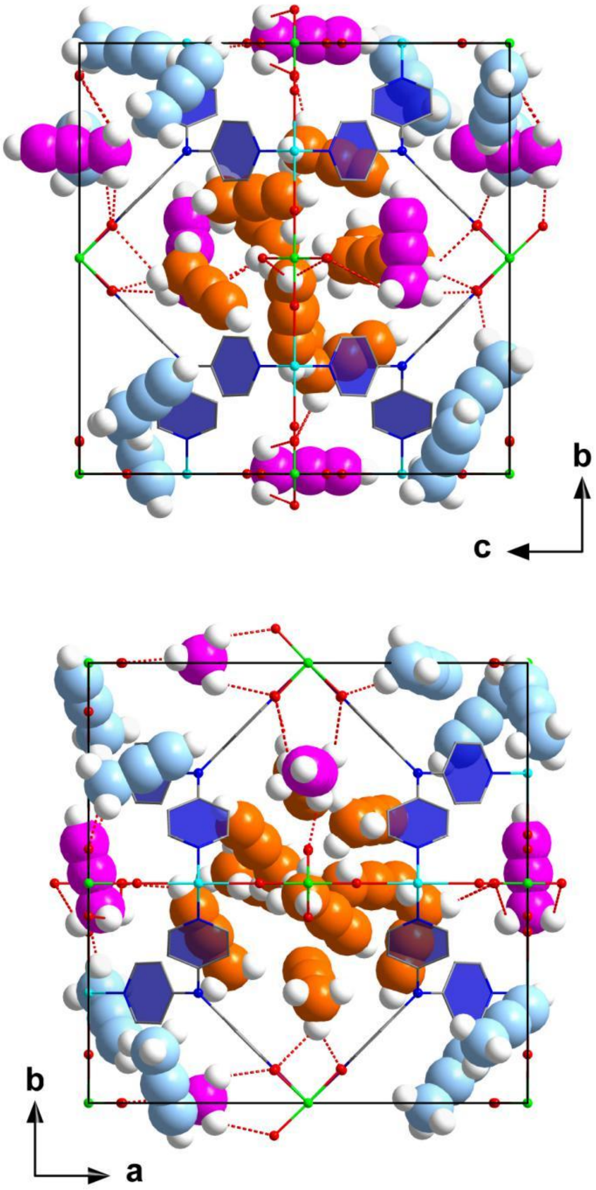

Figure S37. The GCMC optimized adsorption configuration of twenty-five C_3H_4 molecules in the unit cell.(pink: in the channel, orange: in the first cage, blue: in the other cages)

V Breakthrough simulations and experiments

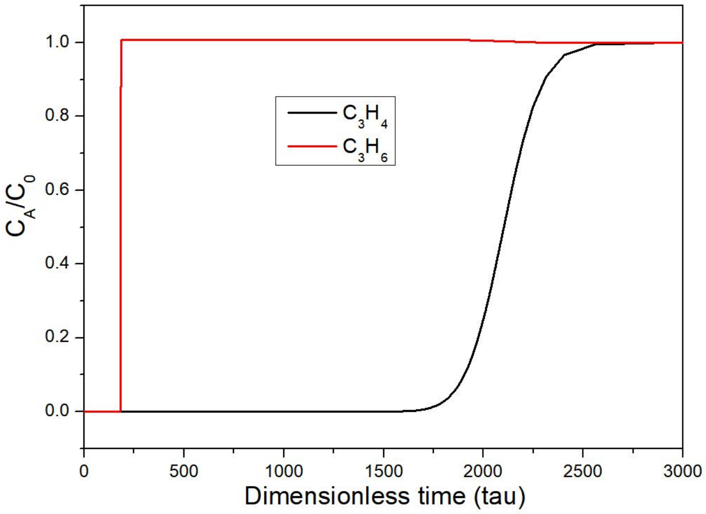

Figure S38. Simulated breakthrough curves of ZNU-2 for C_3H_4/C_3H_6 (10/90) at 298 K.

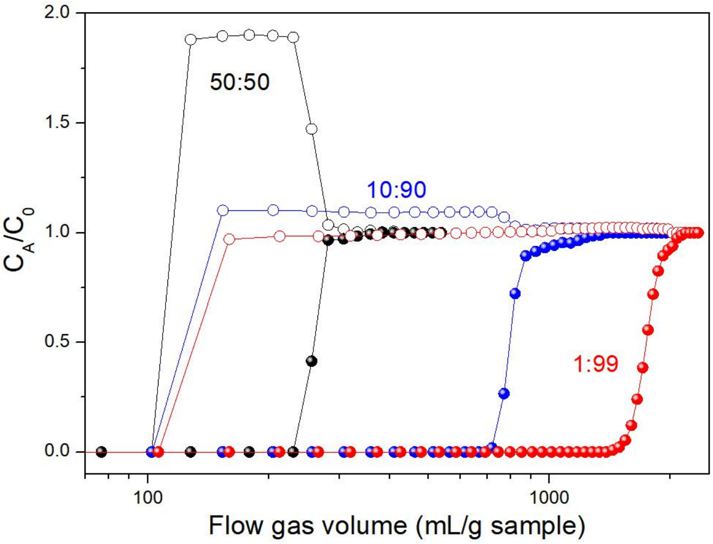

Figure S39. Comparison of the experimental dynamic breakthrough curves of ZNU-2. Breakthrough for C_3H_4/C_3H_6 with different ratios. Breakthrough conditions: flow rate 4 mL/min at 298 K.

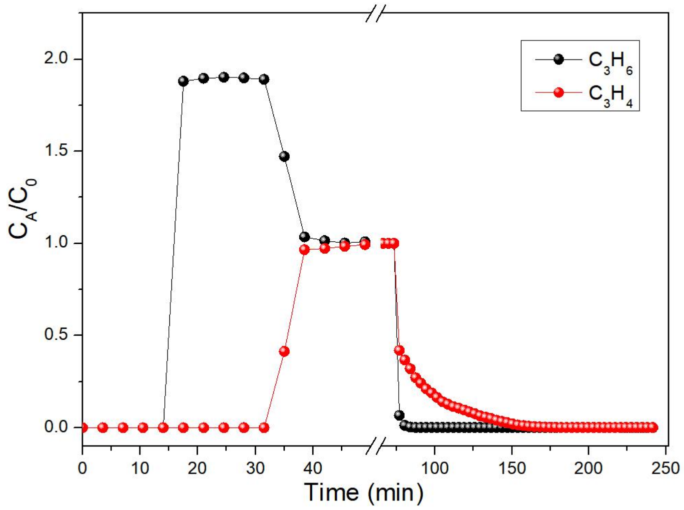

Figure S40. Experimental dynamic breakthrough and desorption curves of ZNU-2. Breakthrough conditions: flow rate of C_3H_4/C_3H_6 (50/50) 4 mL/min at 298 K; desorption conditions: 75 °C Ar purge, 5 mL/min.

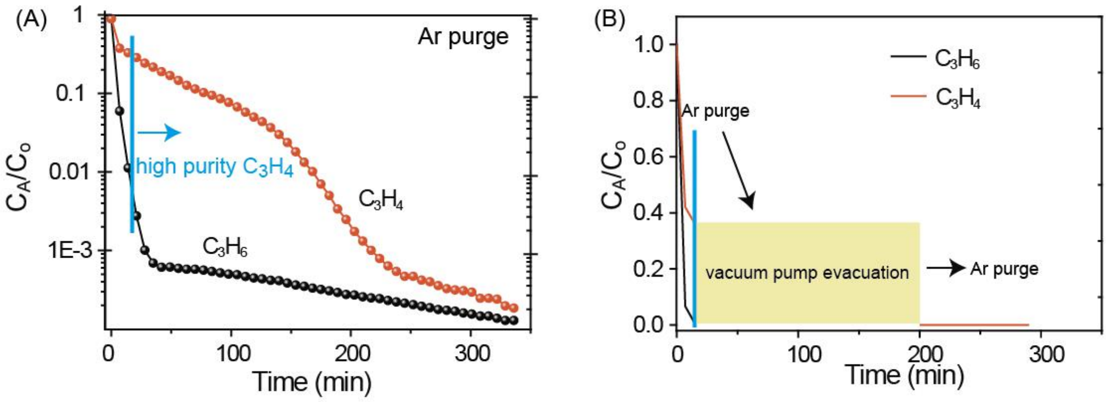

Figure S41. Recovery of high purity C_3H_4 by stepped desorption. (A) Experimental dynamic desorption curves of ZNU-2 after breakthrough experiments of C_3H_4/C_3H_6 (50/50). Desorption conditions: Ar flow rate 5 mL/min at 75 °C. From t = 15 min on, the purity of C_3H_4 desorbed from the column is > 99%. (B) From t =15 min on, Ar purge stopped and vacuum pump evacuation started (see Figure S1D for the equipment operation). At t = 200 min, pump was closed and Ar purge restarted, no C_3H_4 or C_3H_6 was detected, indicating all the C_3H_4 with a small amount of impurity C_3H_6 was recovered by such a VSA process.

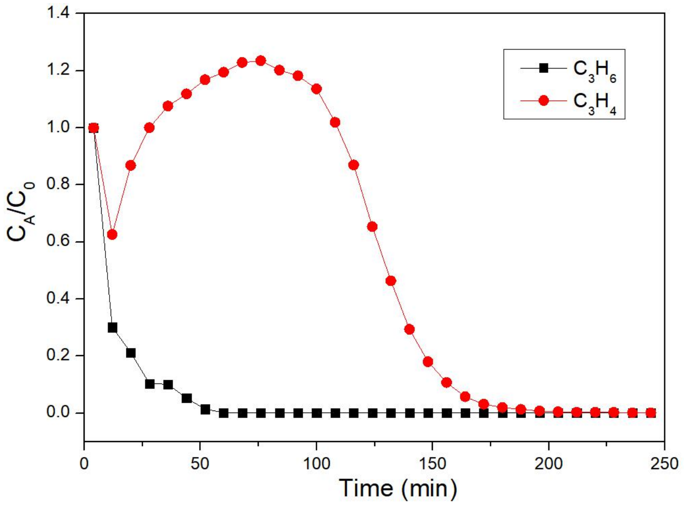

Figure S42. Experimental dynamic desorption curves of ZNU-2 after breakthrough experiment of C_3H_4/C_3H_6 (1/99). Desorption conditions: Ar flow rate 7 mL/min at 75 °C.

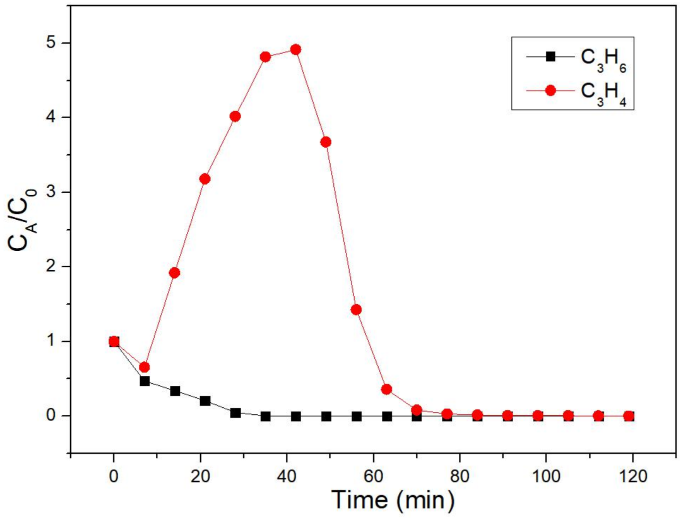

Figure S43. Experimental dynamic desorption curves of ZNU-2 after breakthrough experiment of C_3H_4/C_3H_6 (1/99). Desorption conditions: Ar flow rate 5 mL/min at 120 °C.

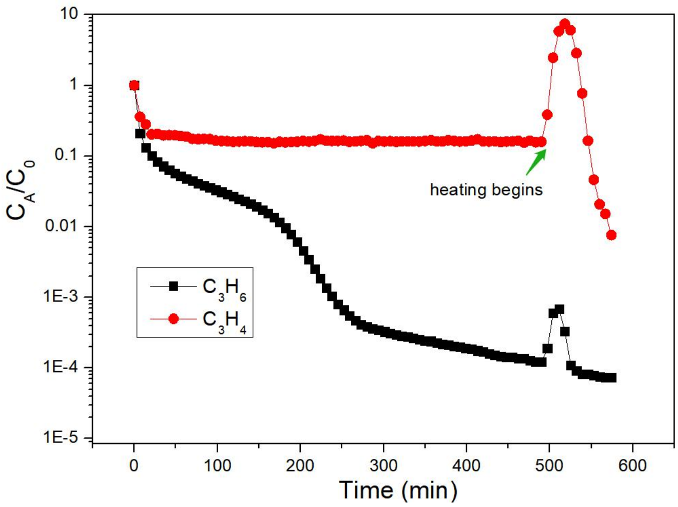

Figure S44. Experimental dynamic desorption curves of ZNU-2 after breakthrough experiment of C_3H_4/C_3H_6 (1/99). Desorption conditions: Ar flow rate 5 mL/min at 25 °C for 480 min and then heating begins; the temperature rises to 120 °C within ~ 10 mins..

VI Comprehensive comparison in hexagonal radar charts

Table S13. Grading scale of the hexagonal radar charts.

	Points				
	1	**2**	**3**	**4**	**5**
q (1kPa)	< 2.0 mmol/g	2.0-2.5 mmol/g	2.5-3.0 mmol/g	3.0-3.5 mmol/g	> 3.5 mmol/g
q (100 kPa)	< 3.0 mmol/g	3.0-4.5 mmol/g	4.5-6.0 mmol/g	6.0-7.5 mmol/g	> 7.5 mmol/g
IAST selectivity	< 5	-	5-10	10-100	> 100
air/water stability	not stable in humid air	-	stable in humid air	stable in water	stable in acid or base
thermal stability	< 200 ℃	-	200~300 ℃	-	> 300 ℃
Q_{st}	> 60 kJ/mol	55-60 kJ/mol	50-55 kJ/mol	45-50 kJ/mol	< 45 kJ/mol

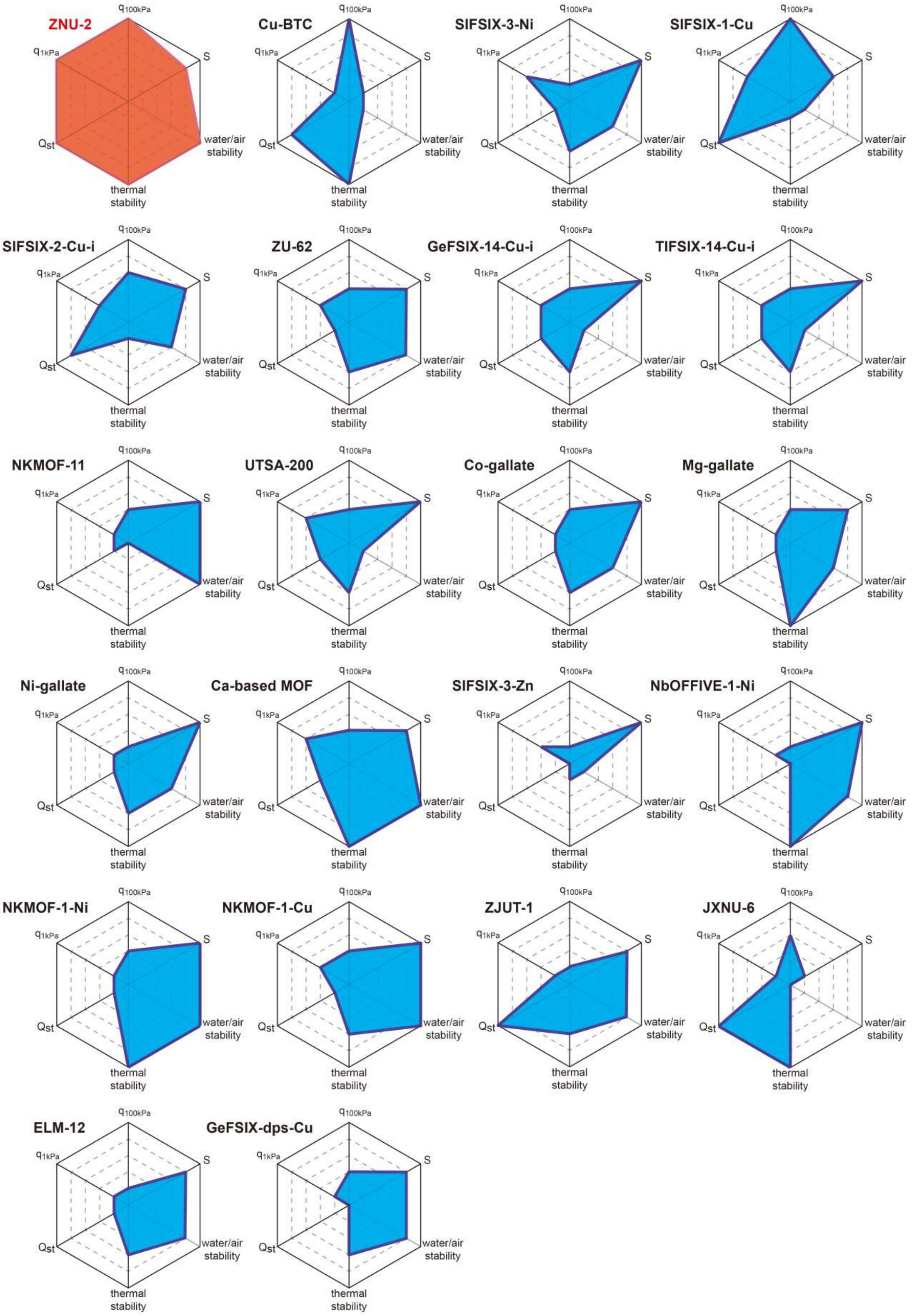

Figure S45. Radar charts for comprehensive evaluation of MOFs on the C_3H_4 storage, C_3H_4/C_3H_6 separation performance and stability.

Table S14. Comparison of the reported materials on C_3H_4 adsorption capacity at 1 kPa, 10 kPa and 100 kPa, and IAST selectivity towards C_3H_4/C_3H_6.

	C_3H_4 uptake (mmol/g)			Selectivity 1:99	Ref
	1 kPa	10kPa	100kPa		
ELM-12	1.83	2.54	2.74	84	[13]
ZJUT-1	0.35	1.07	2.28	70	[17]
NKMOF-11	1.78	2.12	3.10	1074	[18]
JXNU-6	0.36	2.59	5.07	3.1	[19]
NbOFFIVE-1-Ni	1.70	1.72	1.89	882	[3]
UTSA-200	2.99	3.30	3.62	20000	[8]
NKMOF-1-Ni	1.85	2.38	3.50	630.4[a]	[24]
NKMOF-1-Cu	2.03	2.35	3.33	610.5[a]	[24]
GeFSIX-dps-Cu	0.41	3.1	3.73	39.24[b]	[26]
HOF-30	1.15	1.79	2.67	7.7	[31]
Co-gallate	1.21	2.23	3.20	152	[27]
Mg-gallate	1.15	2.70	3.74	65	[27]
Ni-gallate	0.82	1.82	2.64	113	[27]
Ca-based MOF	2.60	2.79	3.18	38[c]	[28]
MIL-100 (Cr)	1.52	4.98	14.52	4.5	[8]
ZIF-8	0.13	1.44	6.28	1.9	[8]
Cu-BTC	1.47	8.17	10.48	3.2	[8]
SIFSIX-3-Zn	2.05	2.11	2.26	115	[3]
ZU-16-Co	2.45	2.47	2.58	248	[32]
TIFSIX-3-Ni	1.86	1.91	2.11	>10^6	[32]
SIFSIX-1-Cu	2.79	6.82	8.72	8.97	[3]/This work
SIFSIX-2-Cu-i	2.21	3.48	4.51	30.58	[3,9,5]/This work
SIFSIX-3-Ni	2.73	2.79	2.97	242.06	[3]/This work
ZU-62	2.28	3.02	3.63	46.31	[5]/This work
SIFSIX-14-Cu-i	2.27	2.95	3.59	112.86	This work
TIFSIX-14-Cu-i	2.19	3.04	3.86	306.12	[9]/This work
GeFSIX-14-Cu-i	2.34	2.97	3.36	240.14	[9]/This work
ZNU-2	**3.9**	**6.18**	**7.7**	**12.5/13.7[b]/16.2[d]**	**This work**

[a] propyne/propylene: 0.5/99; [b] propyne/propylene: 10/90; [c] propyne/propylene: 0.5/99.5; [d] propyne/propylene: 50/50

UTSA-200 and SIFSIX-14-Cu-i feature the same crystal structures. However, as Li et al[8] claimed, the preparation of UTSA-200 needs careful control of the reaction condition and a small amount of impurities are easily produced during the production of UTSA-200, which would greatly affect the separation performance. Thus, for clarity, UTSA-200 refers to the material with slightly better performance reported by Li[8] and SIFSIX-14-Cu-i refers to our synthesized material in this work which is also true in the main text.

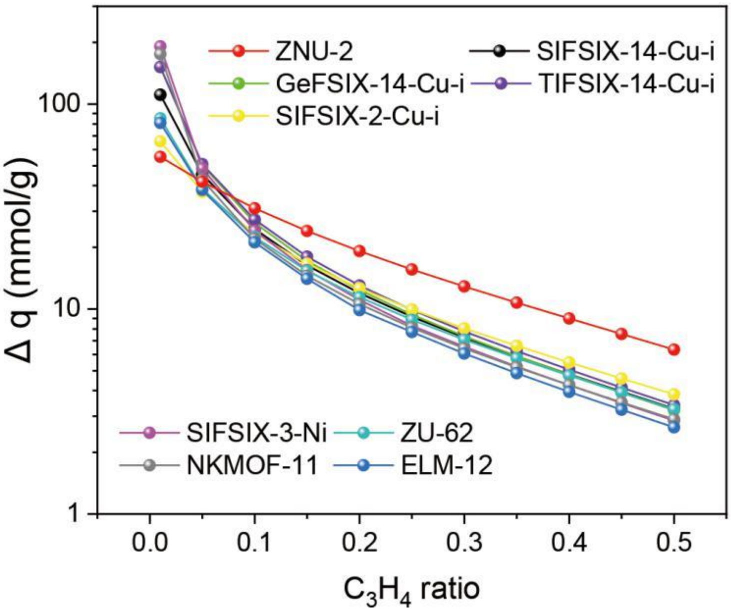

Figure S46. Comparison of the IAST based separation potential for C_3H_4/C_3H_6 mixtures in different proportions in ZNU-2 and reported top performing MOFs.

Table S15. Comparison of the reported materials on C_3H_4 adsorption enthalpy (Q_{st})

	Q_{st} (kJ/mol)	Ref
ELM-12	60.6	[13]
ZU-62	121.9/71	[5, 28]
SIFSIX-2-Cu-i	82.0/46.0	[3,5]
ZJUT-1	33.6	[17]
NKMOF-11	85.0	[18]
JXNU-6	40.0	[19]
SIFSIX-1-Cu	37.2	[3]
SIFSIX-3-Ni	68.0	[3]
UTSA-200	55.3	[8]
NKMOF-1-Ni	65.1	[28]
NKMOF-1-Cu	67.2	[28]
Co-gallate	82.1	[27]
Mg-gallate	66.8	[27]
Ni-gallate	84.4	[27]
Ca-based MOF	55.4	[28]
Cu-BTC	46.0	[33]
ZNU-2	43.0	this work

Table S16 Comparison of the stability of ZNU-2 with other reported materials in the context of C_3H_4/C_3H_6 separation .

Materials	thermal stability (℃)	air stability	stability in humid air	water stability	stability in acid	stability in base	cycling stability	Ref
ELM-12	295	-	-	√	-	-	√	[11-13]
ZU-62	230	√	√	√	-	-	√	[5,14]
SIFSIX-2-Cu-i	170	√	√	×	-	-	√	[2,10,15-16]
ZJUT-1	232	√	√	√	-	-	√	[17]
GeFSIX-14-Cu-i	220	-	×	×	-	-	√	[9-10]
TIFSIX-14-Cu-i	230	-	-	-	-	-	√	[9]
NKMOF-11	-	-	√	√	√	√	√	[18]
JXNU-6	365	-	-	-	-	-	-	[19]
SIFSIX-1-Cu	150	-	×	×	-	-	√	[1,3,15]
SIFSIX-3-Ni	264	√	√	×	-	-	√	[3,15]
SIFSIX-3-Zn	157	-	×	×	-	-	√	[2,4,20]
NbOFFIVE-1-Ni	303	-	√	√	-	-	√	[21-23]
UTSA-200	201	-	×	×	-	-	√	[7-8,15]
NKMOF-1-Ni	382	√	√	√	√	√	√	[24-25]
NKMOF-1-Cu	214	√	√	√	√	√	-	[24-25]
GeFSIX-dps-Cu	214	√	√	√	-	-	√	[26]
Co-gallate	276	√	-	-	-	-	√	[27]
Mg-gallate	401	√	-	-	-	-	-	[27]
Ni-gallate	290	√	-	-	-	-	-	[27]
Ca-based MOF	520	√	√	√	√	√	-	[28]
Cu-BTC	306	√	×	×	-	-	√	[29-30, 33]
ZNU-2	**308**	**√**	**√**	**√**	**√**	**√**	**√**	**this work**

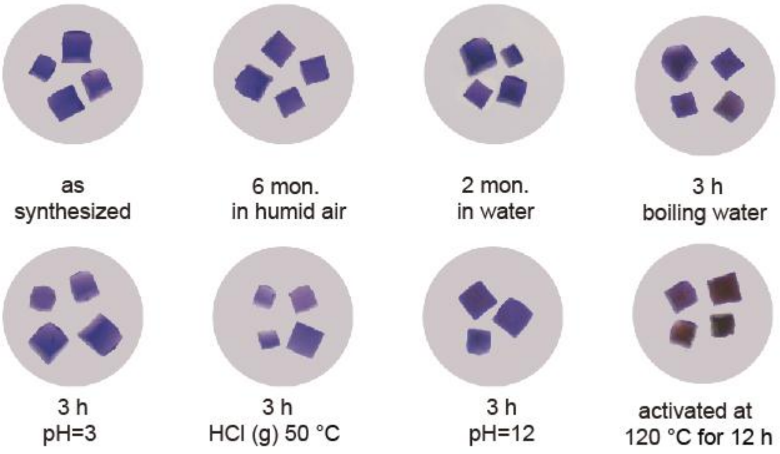

Figure S47. Photographs of single crystals of ZNU-2 after different treatment showing the high stability of ZNU-2 after exposure to humid air, cold water, boiling water, acid water, basic water, acid vapor and 120 °C heating under vacuum.

To provide straightforward evidence, we take photographs of the single crystals of ZNU-2 after different treatment. As shown, the single crystals are still in high quality after leaving in humid air for 6 months, soaking in water for 2 months, soaking in acidic, basic, boiling water or exposure to humid HCl vapor at 50 °C for 3h. Heating at 120 °C under vacuum provides desolvated ZNU-2 with slight color change yet still retains the same crystal structure as indicated by single crystal XRD analysis.

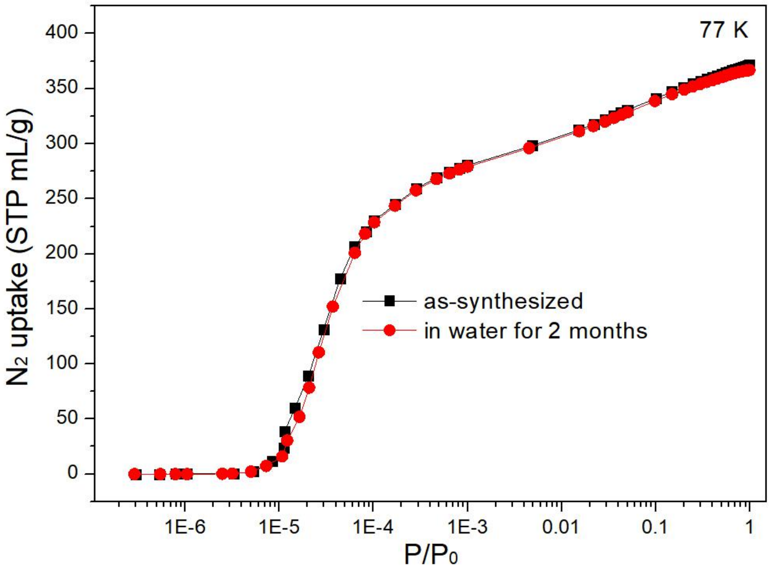

Figure S48. The adsorption isotherm of N_2 at 77 K on as-synthesized ZNU-2 and ZNU-2 after soaking in water for 2 months.

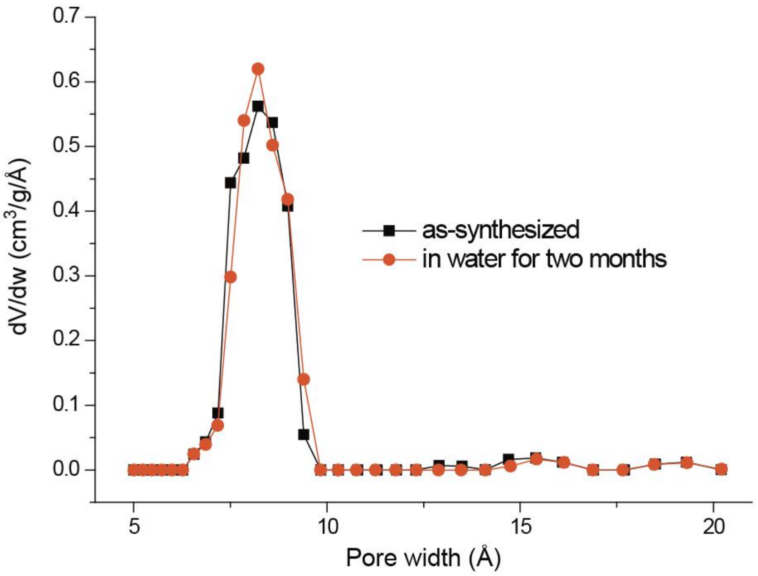

Figure S49. The comparison of the pore width distribution between the as-synthesized ZNU-2 and ZNU-2 after soaking in water for 2 months.

The BET surface area calculated from the N_2 adsorption isotherms under the pressure range of $P/P_0 = 0.01\text{-}0.05$ for ZNU-2 after soaking in water for 2 months is 1369 m^2/g.

MBET summary: Slope = 2.542; Intercept = 9.926×10^{-4}; Correlation coefficient, r= 0.999996; C constant = 2582.296.

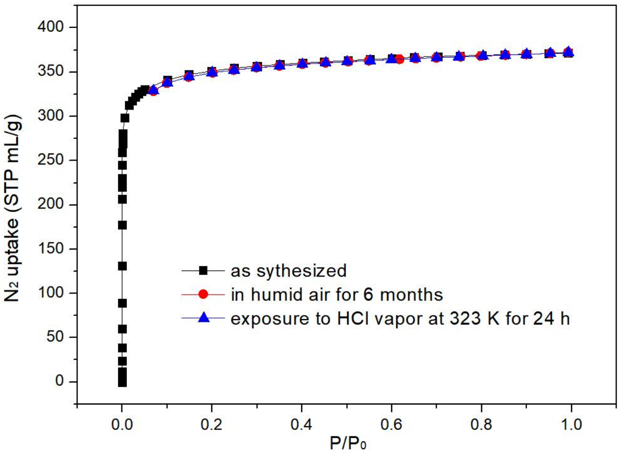

Figure S50. The adsorption isotherm of N_2 at 77 K on as-synthesized ZNU-2 (black), ZNU-2 after exposure to humid air for 6 months (red) and ZNU-2 after exposure to humid HCl vapor at 323 K for 24 h.

All the N_2 adsorption isotherms at 77 K are very close to each other, indicating the high chemical stability of ZNU-2.

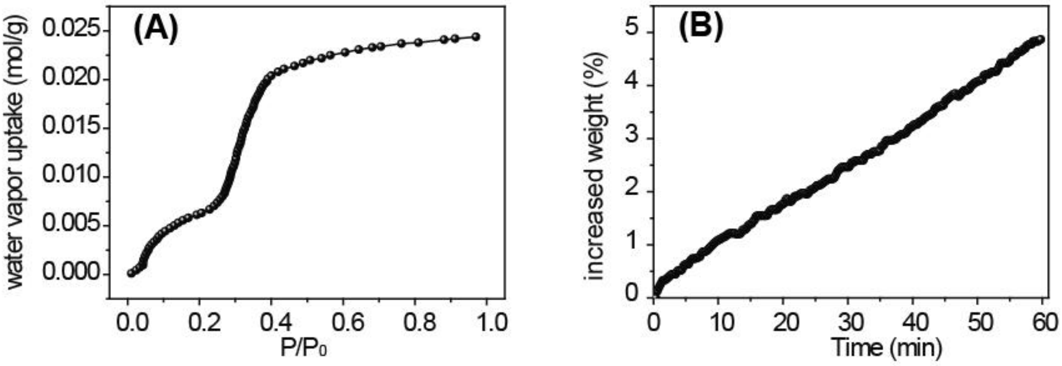

Figure S51. Water vapor adsorption in ZNU-2. (A) Water adsorption isotherms at 298 K (P_0 = 3.169 kPa). (B) Time dependant water adsorption curves at 298 K within 60 mins.

Analysis: ZNU-2 with TiF_6^{2-} anions and large pore volume are not hydrophobic. It can adsorb 0.0244 mol/g (439 mg/g) of water molecules under 298 K and saturated pressure. However, the slope of adsorption isotherms were very flat under low pressure compared to that of C_3H_4 and C_3H_6, indicating the low affinity of ZNU-2 to water vapors. Besides, time dependant water adsorption curves indicated that the water adsorption kinetic within the pores of ZNU-2 is very low. Only 4.9% weight increase was observed within 60 min, which is only ~11% of the saturated amount, indicative of the very slow diffusion of water vapors in the pores of ZNU-2 compared to that of C_3H_4, which reaches equilibrium within 15 mins. Therefore, combined the low affinity of ZNU-2 towards water vapor as well as the extremely slow diffusion of water vapor inside ZNU-2, the influence of water vapor for dynamic C_3H_4/C_3H_6 separation is negligible, which is confirmed by the practical breakthrough experiments in Figure 4G.

Hexagonal radar charts referenced from table tennis games:

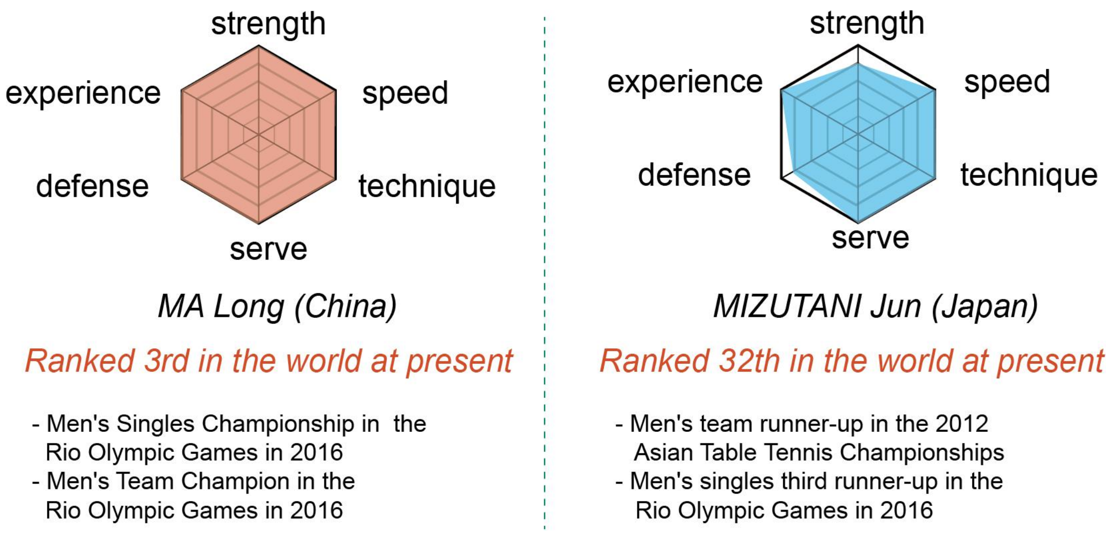

Figure S52. The Hexagonal radar charts in table tennis game to compare two famous players MA long and MIZUTANI Jun.

Japanese media often use hexagonal radar charts to display the strengths and weaknesses of table tennis players. The six sides show ***strength***, ***serve***, ***defense***, ***speed***, ***technique*** and ***experience***. Ma Long, captain of China's men's national table tennis team, received perfect scores in those six areas and has no weaknesses. As such, the table tennis sensation is dubbed "hexagon warrior." As there's a "Long" (dragon in Chinese) in the legendary player's name, Japanese media also call him "the strongest destructive dragon in the world of table tennis” to show his reign of terror.

Reference:
https://www.shine.cn/feature/art-culture/2109034495/#:~:text=hexagon%20warrior%20%E2%80%93%20Ma%20Long%20Japanese%20media%20often,in%20those%20six%20areas%20and%20has%20no%20weaknesses.

VII Reference

[1] S. Noro, R. Kitaura, M. Kondo, S. Kitagawa, T. Ishii, H. Matsuzaka, M. Yamashita, *J. Am. Chem. Soc.,* **2002**, *124*, 2568–2583.

[2] X. Cui, K. Chen, H. Xing, Q. Yang, R. Krishna, Z. Bao, H. Wu, W. Zhou, X. Dong, Y. Han, B. Li, Q. Ren, M. J. Zaworotko, B. Chen, *Science,* **2016**, *353*, 141-144.

[3] L. Yang, X. Cui, Q. Yang, S. Qian, H. Wu, Z. Bao, Z. Zhang, Q. Ren, W. Zhou, B. Chen, H. Xing, *Adv. Mater.,* **2018**, *30,* 1705374.

[4] P. Nugent, Y. Belmabkhout, S. D. Burd, A. J. Cairns, R. Luebke, K. Forrest, T. Pham, S. Ma, B. Space, L. Wojtas, M. Eddaoudi, M. J. Zaworotko, *Nature,* **2013**, *495*, 80-84.

[5] L. Yang, X. Cui, Z. Zhang, Q. Yang, Z. Bao, Q. Ren, H. Xing, *Angew. Chem. Int. Ed.,* **2018**, *57*, 13145-13149.

[6] A. Kumar, D. G. Madden, M. Lusi, K. J. Chen, E. A. Daniels, T. Curtin, J. J. t. Perry, M. J. Zaworotko, *Angew. Chem. Int. Ed.,* **2015**, *54*, 14372-14377.

[7] B. Li, X. Cui, D. O'Nolan, H. M. Wen, M. Jiang, R. Krishna, H. Wu, R. B. Lin, Y. S. Chen, D. Yuan, H. Xing, W. Zhou, Q. Ren, G. Qian, M. J. Zaworotko, B. Chen, *Adv. Mater.,* **2017**, *29*, 1704210.

[8] L. Li, H. M. Wen, C. He, R. B. Lin, R. Krishna, H. Wu, W. Zhou, J. Li, B. Li, B. Chen, *Angew. Chem. Int. Ed.,* **2018**, *57*, 15183-15188.

[9] L. Yang, X. Cui, Y. Zhang, Q. Yang, H. Xing, *J. Mater. Chem. A,* **2018**, *6*, 24452-24458.

[10] Z. Zhang, Q. Yang, X. Cui, L. Yang, Z. Bao, Q. Ren, H. Xing, *Angew. Chem. Int. Ed.,* **2017**, *56*, 16282-16287.

[11] A. Kondo, H. Noguchi, L. Carlucci, D. M. Proserpio, G. Ciani, H. Kajiro, T. Ohba, H. Kanoh, K. Kaneko, *J. Am. Chem. Soc.,* **2007**, *129*, 12362-12363.

[12] F. J. Sotomayor, C. M. Lastoskie, *Microporous Mesoporous Mater.,* **2020**, *292*.

[13] L. Li, R. B. Lin, R. Krishna, X. Wang, B. Li, H. Wu, J. Li, W. Zhou, B. Chen, *J. Am. Chem. Soc.,* **2017**, *139*, 7733-7736.

[14] Q. Wang, T. Ke, L. Yang, Z. Zhang, X. Cui, Z. Bao, Q. Ren, Q. Yang, H. Xing, *Angew. Chem. Int. Ed.,* **2020**, *59*, 3423-3428.

[15] D. O'Nolan, A. Kumar, M. J. Zaworotko, *J. Am. Chem. Soc.,* **2017**, *139*, 8508-8513.

[16] L. Yang, A. Jin, L. Ge, X. Cui, H. Xing, *Chem. Commun.,* **2019**, *55*, 5001-5004.

[17] H.-M. Wen, L. Li, R.-B. Lin, B. Li, B. Hu, W. Zhou, J. Hu, B. Chen, *J. Mater. Chem. A,* **2018**, *6*, 6931-6937.

[18] Y.-L. Peng, T. Wang, C. Jin, P. Li, S. Suepaul, G. Beemer, Y. Chen, R. Krishna, P. Cheng, T. Pham, B. Space, M. J. Zaworotko, Z. Zhang, *J. Mater. Chem. A,* **2021**, *9*, 2850-2856.

[19] Z. T. Lin, Q. Y. Liu, L. Yang, C. T. He, L. Li, Y. L. Wang, *Inorg. Chem.,* **2020**, *59*, 4030-4036.

[20] S. S. Meng, Z. R. Tao, W. Q. Tang, T. Han, Y. Du, Z. Y. Gu, *J. Chromatogr. A,* **2020**, *1632*, 461604.

[21] P. M. Bhatt, Y. Belmabkhout, A. Cadiau, K. Adil, O. Shekhah, A. Shkurenko, L. J. Barbour, M. Eddaoudi, *J. Am. Chem. Soc.,* **2016**, *138*, 9301-9307.

[22] M. Khraisheh, F. Almomani, G. Walker, *Catalysts,* **2021**, *11*, 510.

[23] K. Chen, K. Xu, L. Xiang, X. Dong, Y. Han, C. Wang, L.-B. Sun, Y Pan, *J. Membr. Sci.*, **2018**, *563*, 360-370.

[24] Y. L. Peng, C. He, T. Pham, T. Wang, P. Li, R. Krishna, K. A. Forrest, A. Hogan, S. Suepaul, B. Space, M. Fang, Y. Chen, M. J. Zaworotko, J. Li, L. Li, Z. Zhang, P. Cheng, B. Chen, *Angew. Chem. Int. Ed.,* **2019**, *58*, 10209-10214.

[25] Y. L. Peng, T. Pham, P. Li, T. Wang, Y. Chen, K. J. Chen, K. A. Forrest, B. Space, P. Cheng, M. J. Zaworotko, Z. Zhang, *Angew. Chem. Int. Ed.,* **2018**, *57*, 10971-10975.

[26] T. Ke, Q. Wang, J. Shen, J. Zhou, Z. Bao, Q. Yang, Q. Ren, *Angew. Chem. Int. Ed.,* **2020**, *59*, 12725-12730.

[27] Z. Li, L. Li, L. Guo, J. Wang, Q. Yang, Z. Zhang, Y. Yang, Z. Bao, Q. Ren, *Ind. Eng. Chem. Res.,* **2020**, *59*, 13716-13723.

[28] L. Li, L. Guo, F. Zheng, Z. Zhang, Q. Yang, Y. Yang, Q. Ren, Z. Bao, *ACS Appl. Mater. Interfaces,* **2020**, *12*, 17147-17154.

[29] S. Xu, X. Guo, Z. Qiao, H. Huang, C. Zhong, *Ind. Eng. Chem. Res.,* **2020**, *59*, 12451-12457.

[30] Y. Sun, Z. Ke, Y. Tang, S. Wang, Y. Wu, Q. Xia, Z. Li, *Ind. Eng. Chem. Res.,* **2020**, *59*, 6202-6209.

[31] B. Yu, S. Geng, H. Wang, W. Zhou, Z. Zhang, B. Chen, J. Jiang, *Angew. Chem. Int. Ed.,* **2021**, *60*, 25942-25948.

[32] Z. Zhang, Q. Ding, J. Cui, X. Cui, H. Xing, *Small,* **2020**, *16*, 2005360.

[33] Y. L. Peng, T. Wang, C. Jin, C. H. Deng, Y. Zhao, W. Liu, K. A. Forrest, R. Krishna, Y. Chen, T. Pham, B. Space, P. Cheng, M. J. Zaworotko, Z. Zhang, *Nat. Commun.,* **2021**, *12*, 5768.